Morphoevolution of the Seymareh landslide-dam lake system (Zagros Mountains, Iran): Implications for Holocene climate and environmental changes

6 authors, including:

Michele Delchiaro
Sapienza University of Rome
16 PUBLICATIONS **35** CITATIONS

SEE PROFILE

Giulia Iacobucci
Sapienza University of Rome
8 PUBLICATIONS **10** CITATIONS

SEE PROFILE

Francesco Troiani
Sapienza University of Rome
64 PUBLICATIONS **779** CITATIONS

SEE PROFILE

Marta Della Seta
Sapienza University of Rome
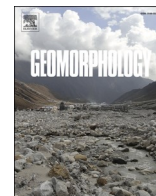**133** PUBLICATIONS **1,751** CITATIONS

SEE PROFILE

Some of the authors of this publication are also working on these related projects:

Sviluppo dei sistemi sostenibile geotermici Associati della ai sistemivulcanici Puna di nelle Salta Province View project

Deciphering Mantle Contribution on Surface uplift in the Atlas-Meseta system (Morocco) View project

Morphoevolution of the Seymareh landslide-dam lake system (Zagros Mountains, Iran): Implications for Holocene climate and environmental changes

Michele Delchiaro [a,*], Giulia Iacobucci [a], Francesco Troiani [a], Marta Della Seta [a], Paolo Ballato [b], Luca Aldega [a]

[a] Department of Earth Sciences, Sapienza University of Rome, Rome, Italy
[b] Department of Sciences, Roma Tre University, Rome, Italy

ABSTRACT

The Seymareh landslide is the largest rock slope failure (44 Gm^3) ever recorded on the exposed Earth surface. It detached at ~10 ka from the northeastern flank of the Kabir-Kuh anticline (Zagros Mountains, Iran) creating a natural dam responsible for the formation of a lake system that persisted for ~3 kyr during the early and mid-Holocene before its emptying phase caused by overflow. The chronology of its demise and connection to the Holocene climate variations have been barely studied. To reconstruct the influence of local vs. regional environmental changes upon the lake history and unravel their contribution on the lake overflowing phase, we analyzed 13 samples extracted from a 30-m-thick lacustrine succession belonging to Seymareh Lake. We performed grain size analysis, carbon and oxygen stable isotopes of carbonate-bearing sediments, and X-ray diffraction analysis of clay minerals, in addition to the geomorphological analysis to reconstruct the lake system morphoevolution. Main results highlight that the lake infilling phase was characterized by a first period (from 9.73 ± 0.13 to 7.37 ± 0.73 ka) with a median sedimentation rate of ~2 cm yr^{-1} and a second period (from 7.37 ± 0.73 to 6.98 ± 0.39 ka) marked by an increased sedimentation rate up to ~10 cm yr^{-1}. The age of 6.98 ± 0.39 ka is here considered as the termination of lacustrine sedimentation and the beginning of lake emptying and new valley entrenchment. Stable isotope and X-ray diffraction analyses confirm a stable humid interval after the early-mid Holocene arid to humid transition, consistent with other regions of the Middle East. During this transition, rainfall seasonality and its inter-annual irregularity may have prevented the development of a widespread vegetation cover that likely favored the increase of denudation rates on hillslopes and sediment supply along connected channels network. Therefore, the sedimentation rate increased within the downstream lake basin. However, in the late infilling phase from ~7.6–7.32 ka, local high energy hydroclimatic events, characterized by high sand content and low δ^{18}O concentration, were recorded more frequently. This could justify a sudden increase in the tributaries' discharge that culminated at ~7.3 ka because of the complete overflow of Jaidar Lake into Seymareh Lake likely causing the overflowing of the entire Seymareh landslide-dam lake system.

1. Introduction

Environmental variability is recognized worldwide as a fundamental factor for generating disequilibrium conditions in geomorphic systems, including hillslopes, and connected channel networks (Collison et al., 2000; Crozier, 2010; Huggel et al., 2012; Alvioli et al., 2018; Harrison et al., 2018; Pánek, 2019). The morphodynamics of the hillslope-channel system during environmental changes is extremely relevant

for establishing hillslope instability conditions (Crozier, 2010; Huggel et al., 2012; Wu et al., 2020), the potential development of valley-blocking landslides (Clague and Evans, 2000; Korup, 2002; Hermanns et al., 2004; Costa and Díaz, 2007; Fan et al., 2020) as well as the evolution and extinction of associated landslide-dam lakes (Ermini and Casagli, 2003; Savelli et al., 2013; Stefanelli et al., 2016; Heidarzadeh et al., 2017; Zhong et al., 2021).

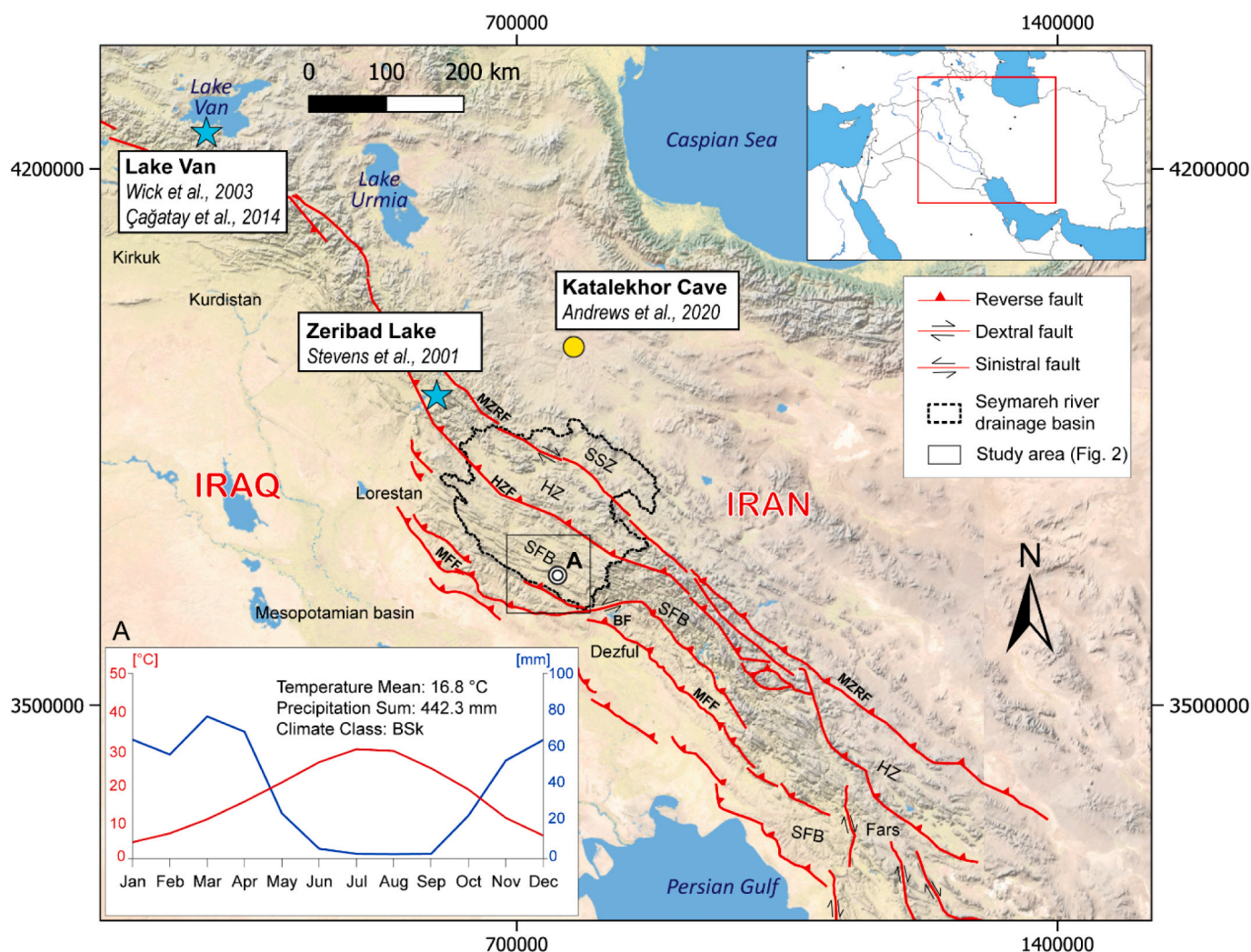Lake overflowing is largely accepted as the main response to

---

* Corresponding author.
 *E-mail address:* michele.delchiaro@uniroma1.it (M. Delchiaro).

Fig. 1. Regional topography of the Zagros and the Iranian Plateau showing the proxy data from available literature (blue star: lacustrine deposit; yellow circle: speleothem) and location of the study area. Climate chart of Poldokhtar village (685 m a.s.l.) for the period 1990–2019 based on data from Harris et al. (2020) in the inset A whose location is reported in the map (A). HZ: High Zagros, SFB: Simply Folded Belt, MFF: Mountain Front Fault, HZF: High Zagros Fault, MZRF: Main Zagros Reverse Fault, and BF: Balarud Fault. The coordinate system is WGS84 UTM 38 N (EPSG: 32638).

variations in water discharge and sediment supply (Costa and Schuster, 1988; Ouimet et al., 2007; Fan et al., 2020) that depend on spatial and temporal changes of environmental conditions. In this regard, environmental transitions, i.e., from arid to humid conditions, can cause an increase of sediment supply from hillslopes and/or water discharge along the channel network, predisposing the downstream lake basins to overflow events (O'Connor and Costa, 2004). Nevertheless, local vs. regional contributions, as well as short- vs. long-term climate changes likely affect the stability of landslide dams and deserve more in-depth analysis. For this reason, lacustrine records offer ideal sedimentary archives for unravelling the evolution of lake basins in response to climate changes, including the evolution of hillslopes and channel networks.

In this paper, we focused on Seymareh Lake, which was generated at ~10 ka by the largest rock slope failure (44 Gm³) ever recorded on the exposed Earth surface, known as the giant Seymareh landslide (Watson and Wright, 1969; Roberts and Evans, 2013; Shoaei, 2014; Delchiaro et al., 2019, 2020; Rouhi et al., 2019, 2022). The Seymareh landslide (33°03′33.13″N, 47°39′52.87″E) detached from the northeastern limb of the Kabir-Kuh anticline (Zagros Mountains, Iran) creating the natural dam responsible for the formation of a three-lake system consisting of Seymareh, Jaidar, and Balmak lakes, with areas of 259, 46, and 5 km², respectively. The endorheic lake system persisted for ~3 ka during the

Holocene before its emptying phase caused by overflow (Delchiaro et al., 2019, 2020). Shoaei (2014) suggested that the Seymareh landslide dam overflow was caused by the high discharge of the Kashkan River into the smaller reservoir of Jaidar Lake that led the latter to drain into Seymareh Lake. In this context, the purpose of this work is to define local vs regional climatic and environmental contributions to the morphoevolution of the Seymareh landslide-dam lake system during early and mid-Holocene times, providing new insights into the impact of climate and environmental changes on the lake and connected hillslope-channel systems before the overflow event.

To achieve the objective, we analyzed a 30-m-thick lacustrine succession from Seymareh Lake with a conventional geomorphological approach aimed at reconstructing the Seymareh landscape evolution by means of the local succession of fluvial terraces, the latter being already studied and chronologically constrained by Delchiaro et al. (2019, 2020). The lacustrine sedimentary succession was studied by a multi-method approach consisting of grain size analysis and statistics, carbon and oxygen stable isotopes of carbonate-bearing sediments, and X-ray diffraction analysis of clay minerals. The main results are discussed in relation to the early and mid-Holocene climate changes and their effect on Earth surface processes in the Middle East.
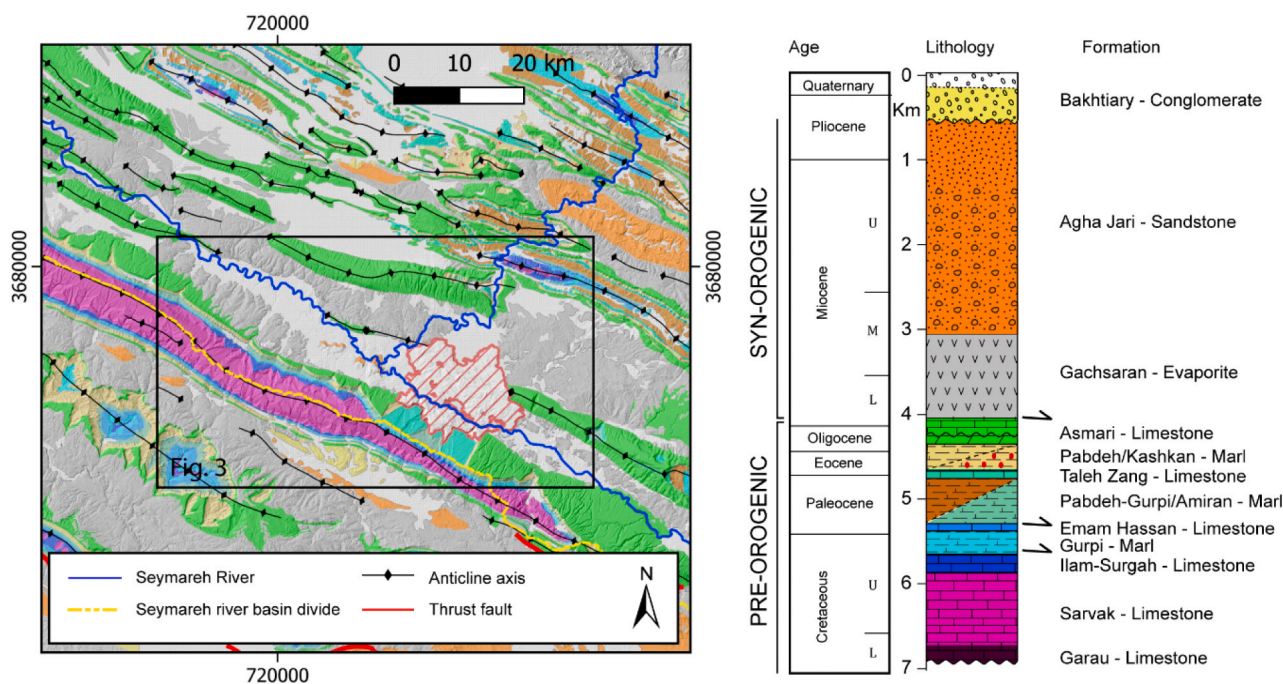
Fig. 2. Geological map of the study area in the Lorestan Province. The hatched area refers to the landslide debris. The geological data are from the National Iranian Oil Company (NIOC) at a scale of 1:100,000 (Llewellyn, 1974; Macleod, 1970; Macleod and Fozoonmayh, 1970; Macleod and Roohi, 1970). The stratigraphic column and main detachment layers in the Luristan region are taken from Casciello et al. (2009) and Sherkati et al. (2006).

Table 1
Samples, dating method, elevation, and age used to constrain the chronological model of the lake infilling phase and overflow.

Sample	Dating method	Description	Elevation (m a.s.l.)	Elevation above river (m)	Age (ka)	Error (ka)
SEY6[a]	OSL	Pre-lacustrine alluvial deposits	570	2	17.9[a]	±1.50
SEY8[a]	OSL	Lacustrine deposits (Lac)	560	20	10.4[a]	±0.90
SEY4[a]	OSL	Lacustrine deposits (Lac)	590	22	7.37[a]	±0.73
TO-13445[b]	[14]C	Lacustrine deposits (Lac)	540	3.5	9.73	±0.13
SEY9[a]	OSL	III order strath terrace	570	120	6.59[a]	±0.49
SEY5[a]	OSL	I order fill terrace (Qt1)	607	37	4.49	±0.48

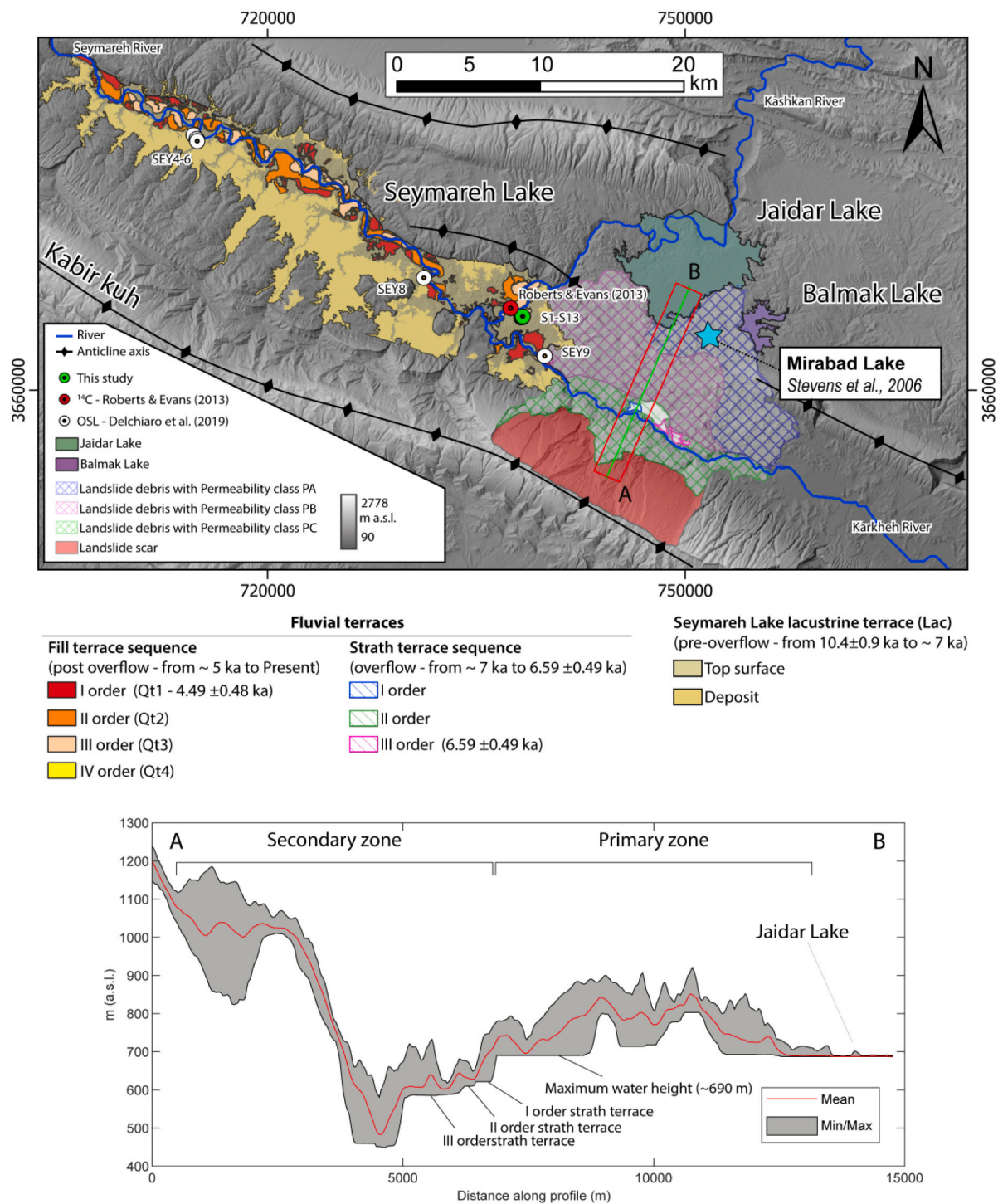[a] Delchiaro et al. (2019).
[b] Roberts and Evans (2013).

2. Regional tectonic and climatic setting

The Seymareh drainage basin (Fig. 1) is located within the northwestern part of the Zagros belt, which resulted from the collision of continental blocks of Arabia and Eurasia and the consequent consumption of the Neotethys since the late Cretaceous (Boutoux et al., 2021; McQuarrie, 2004; Mouthereau et al., 2012; Stampfli and Borel, 2002; Talbot and Alavi, 1996). Its drainage network dissects most of the Lorestan region (e.g., Vergés et al., 2011), crossing several tectonic units of the mountain range, which are oriented from NE to SW: the Sanandaj-Sirjan Zone (SSZ), the High Zagros zone (HZ, named also Imbricate zone), the Simply Folded Belt (SFB) and the continental Mesopotamian Foreland (Agard et al., 2005, and references therein). These tectonic units are bounded by regional faults such as the Main Zagros Reverse Fault (MZRF), the High Zagros Fault (HZF), and the Mountain Front Fault (MFF). The SSZ comprises deformed and metamorphosed Paleozoic to Mesozoic rocks intruded by Upper Cretaceous to Paleocene plutons (Vergés et al., 2011, and references therein). The HZ consists of imbricated tectonic slices involving radiolarite-ophiolite complexes, Mesozoic, and Cenozoic sedimentary and volcanic rocks, and thrust sheets from the SSZ (e.g., Agard et al., 2005). The SFB is characterized by a folded 12–14-km-thick sedimentary cover deposited on the northeastern continental border of the Arabian plate (e.g., Bigi et al., 2018). The sedimentary succession is composed of Upper Paleozoic to Upper

Cretaceous passive margin deposits, and late Cretaceous to present foreland deposits (Casciello et al., 2009; James and Wynd, 1965; Vergés et al., 2011). The 3–4-km-thick Mesozoic succession in the Lorestan province, is dominated by large carbonate platforms and shallow basin lithostratigraphic units made up of limestone, marls, shales, and marly limestones interbedded with episodic plugs of evaporites (Fig. 2). The succession includes the carbonates of the Bangestan Group (Garau, Sarvak and Ilam-Surgah formations), two clastic wedges separated by the early-middle Miocene carbonate of the Asmari Formation (Casciello et al., 2009; Vergés et al., 2011): the proto-Zagros foreland sequence (Paleocene-Early Eocene - Amiran, Taleh Zang, and Kashkan formations) and the Mesopotamian foreland succession (Miocene-early Pleistocene – Gachsaran, Agha Jari and Bakhtiari formations).

The climatic conditions in the Zagros Mountains are mostly controlled by three different climate regimes: (i) the Mediterranean in the west, (ii) the monsoon in the south, and (iii) the continental in the eastern and northern sectors. The area corresponds to the easternmost sector of the ancient Near East Fertile Crescent, where rainfall occurs in winter because of cyclogenesis in the Arabian Sea, Persian Gulf, Red Sea, and northern Indian Ocean (Evans and Smith, 2006; Andrews et al., 2020). The modern Iranian climate is mainly characterized by arid and semiarid conditions, especially in the Iranian plateau where the Caspian and the Mediterranean basins are bounded by the Alborz and Zagros-Bitlis Mountains, respectively. Therefore, the mean annual

Fig. 3. Map of the lacustrine and fluvial terrace sequences and the most significant landforms characterizing the valley morphoevolution after the emplacement of the Seymareh landslide (modified after Delchiaro et al., 2019). Sampling location from this study (green circle) and from available literature (white and red circles) used for the chronological model of lake infill and overflow are reported (see Table 1 for details). The permeability zonation of the landslide debris proposed by Rouhi et al. (2022) is reported. The grey-scale map indicates elevation, which is derived from the 30-m SRTM (Farr et al., 2007). The coordinate system is WGS84 38N (EPSG: 32638). The 2000 m wide swath profile shown in the map is also reported.

precipitation clearly shows a pronounced latitudinal and longitudinal gradient that decreases eastward (Kehl, 2009), causing a cold semiarid climate (BSk) following the Köppen (1900) climate classification. Observing the climate chart of Poldokhtar village in the Lorestan province (Iran) for the period 1990–2019 (Harris et al., 2020) (Fig. 1), autumn and winter are the wettest seasons, with highest precipitation in March (77.6 mm), while summer is dry and hot. The average

temperature of the coldest month (i.e., January) is 4.4 °C and the average summer temperature is above 24 °C, with a peak of 29.5 °C in July.

Table 2
Grain size analysis results and grain size parameters for the Seymareh lacustrine succession.

Sample	Elevation (m a.s.l.)	Grain size analysis (%wt.)				Mean size (Φ)	Mean size (mm)	Standard deviation	Skewness	Kurtosis
		Gravel	Sand	Silt	Clay					
S1	610	0	1	44	55	8.19	0.0034	1.6682	−0.2697	0.6250
S2	608	0	0	45	55	8.14	0.0035	1.7115	−0.2890	0.6092
S3	607	0	49	23	28	5.76	0.0184	2.9656	0.4631	0.6092
S4	605	0	0	36	64	8.62	0.0025	1.4488	−0.5180	0.6798
S5	604	0	0	41	60	8.62	0.0025	1.4488	−0.5180	0.6798
S6	598	0	86	7	6	2.68	0.1553	1.5011	0.3788	3.4002
S7	595	0	46	32	23	5.63	0.0201	2.8888	0.3786	0.6999
S8	592	0	33	45	22	5.85	0.0173	2.8422	0.2421	0.7484
S9	589	0	18	43	40	6.92	0.0082	2.5687	−0.1171	0.5410
S10	585	0	0	42	58	8.36	0.0030	1.5675	−0.3466	0.6335
S11	583	0	25	56	19	5.85	0.0173	2.5119	0.3741	0.9250
S12	582	0	0	47	53	8.12	0.0036	1.6844	−0.2054	0.6142
S13	580	0	1	44	55	8.18	0.0034	1.6737	−0.2584	0.6204

3. The Seymareh landslide and chronological constraints for the valley morphoevolution

The morphoevolution of the Seymareh valley during the early and mid-Holocene, after the emplacement of the valley-blocking landslide, can be reconstructed and chronologically constrained using several available ages (Table 1). Roberts and Evans (2013) dated charcoal fragments yielding an uncalibrated radiocarbon date of 8.71 ± 0.08 ka (TO-13445, Table 1). The corresponding calibrated date using Calib 5.0.2 (Stuiver et al., 1998) is 9.73 ± 0.13 ka. Based on the interpretation of three individual radiocarbon ages provided by Griffiths et al. (2001), a radiocarbon bracket age for the landslide event was suggested between 9.8 and 8.7 ^{14}C ka. Delchiaro et al. (2019) identified different generations of fluvial terraces that were used as geomorphic markers (sensu Burbank and Anderson, 2011) for reconstructing the local valley evolutionary stages after the emplacement of the valley-blocking landslide (Fig. 3). Geomorphic markers are distributed upstream and onto the landslide debris and include: (1) a suite of four generations of fill terraces (named Qt1–Qt4 from the ancient ones) hanging at different heights on the present talweg and entrenched in the terraced lacustrine deposit (Lac); (2) a suite of three strath terraces shaped onto the landslide debris along the Seymareh River gorge.

Upstream of the landslide debris, Delchiaro et al. (2019) dated three sediment samples (SEY6, SEY8, and SEY4 in Table 1) by Optically Stimulated Luminescence (OSL). The age of 17.9 ± 1.5 ka (SEY6) from a fluvial deposit exposed at the base of the lacustrine sediments predated by ca. 7 ka the emplacement of the Seymareh valley-blocking landslide, according to the time constraints for landslide emplacement provided by Roberts and Evans (2013). The lacustrine deposits were dated at two different stratigraphic levels located at 560 and 590 m a.s.l., which provided consistent OSL ages of 10.4 ± 0.9 ka (SEY8) and 7.37 ± 0.73 ka (SEY4), respectively.

Moreover, three levels of strath terraces hanging at different heights on the landslide debris along the Seymareh River gorge represent key geomorphic markers for understanding the development of the landslide dam. Delchiaro et al. (2019) dated the third, lower strath terrace level (SEY9; Table 1), which yielded an age of 6.59 ± 0.49 ka constraining the initial stage of the lake emptying. Finally, an OSL age of 4.49 ± 0.48 ka from the first generation of the fill terraces (i.e., Qt1 fluvial terrace) (sample SEY5 in Table 1) provided a further chronological constraint for the lake emptying phase and ongoing valley entrenchment (Delchiaro et al., 2019).

Recently, Rouhi et al. (2022) proposed a zonation of the landslide debris based on a spatial statistical approach where primary (original) and secondary (modified) regions, respectively, attributed to the original shape of the landslide debris and the one reshaped by fluvial erosion, are distinguished. Permeability tests performed on soil samples taken from the debris surface allowed the authors to validate the model obtaining a permeability zonation consistent with the statistical model. It showed that the high permeability values (PC permeability class) are associated with secondary zones and low values (PA and PB permeability classes) with primary ones (Fig. 3).

4. Materials and methods

A 30-m-thick lacustrine succession from Seymareh Lake was analyzed (samples S1–S13). Samples were collected from 580 to 610 m a.s.l. (Fig. 3 and Supplementary material 1). A multi-proxy analysis has been conducted on the lacustrine sediments, including grain size and scanning electron microscope (SEM) analyses, carbon and oxygen stable isotopes, and X-ray diffraction. A chronological model based on an Age-Elevation plot completes the multi-proxy analysis.

4.1. Grain size and SEM analyses

The grain size analysis was performed to extract information about the energy of the depositional system. During the sampling, particular attention was given to preventing the samples from being contaminated by recent deposits. In this regard, once the site for sampling was identified, it was important to carefully clean off the slope.

Laboratory analysis was carried out following ASTM (2007) recommendations at the Geotechnical Laboratory of Earth Sciences Department of Sapienza University of Rome for interpreting the energy of the sedimentary system. The ASTM 200 sieve passing was characterized with X-ray sedigraphy using SediGraph III by Micromeritics coupled with a multisampler (MasterTech 52) interfaced by management software.

Cumulative curves were built with the results of the grain size analysis. The size is expressed both in *mm* and in Φ, where Φ = log$_2$ (size in *mm*).

From the cumulative curves the following grain size parameters were obtained (Folk and Ward, 1957):

$$Mean\ Size = \frac{\varphi_{16} + \varphi_{50} + \varphi_{84}}{3} \tag{1}$$

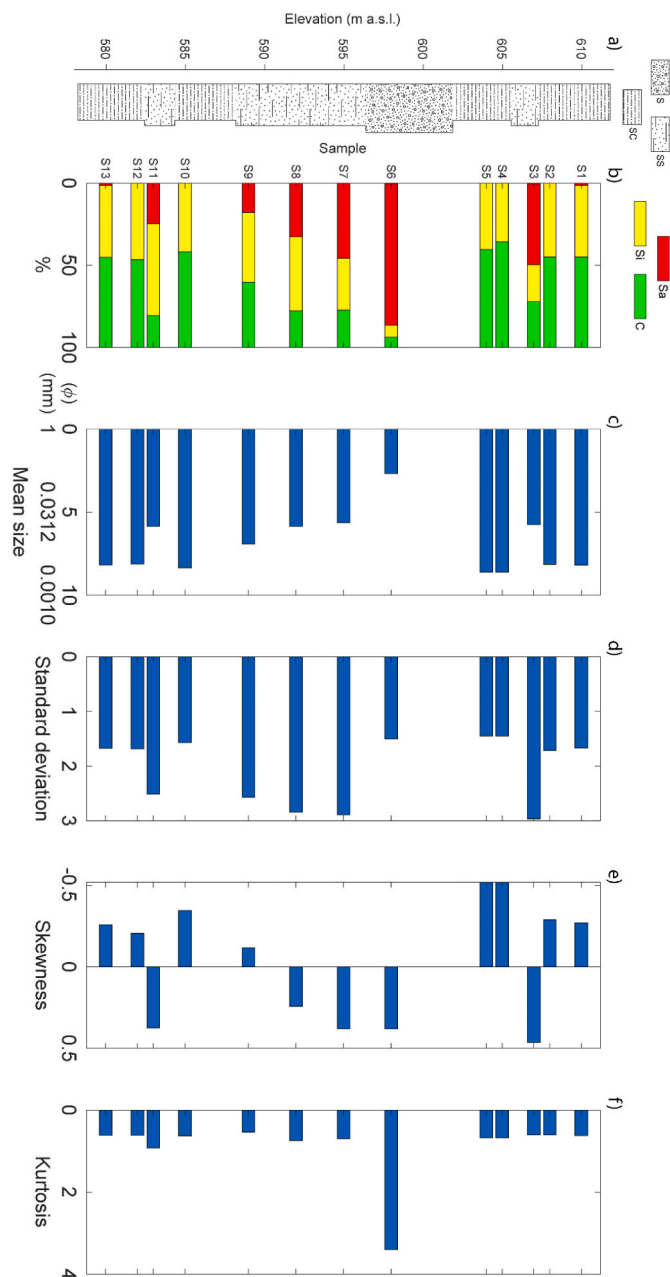$$Standard\ deviation = \frac{\varphi_{84} - \varphi_{16}}{4} + \frac{\varphi_{95} - \varphi_5}{6.6} \tag{2}$$

$$Skewness = \frac{\varphi_{16} + \varphi_{84} - 2\varphi_{50}}{2(\varphi_{84} - \varphi_{16})} + \frac{\varphi_5 + \varphi_{95} - 2\varphi_{50}}{2(\varphi_{95} - \varphi_5)} \tag{3}$$

$$Kurtosis = \frac{\varphi_{95} - \varphi_5}{2.44(\varphi_{75} - \varphi_{25})} \tag{4}$$

where the subscript for ϕ indicates the cumulative percentile values, i.e., the grain size at which the indicated percentage of the grains are coarser.

The *Mean Size* expresses the average width of the grains. The

Fig. 4. Results of the grain size analysis plotted against elevation: a) simplified stratigraphic column of lacustrine succession; b) grain class distribution; c) mean size distribution; d) standard deviation distribution; e) skewness distribution; f) kurtosis distribution. Acronyms: S = coarse sand; SS = sandy silt; SC = silty clay; Sa = sand; Si = silt; C = clay.

Standard Deviation defines the variability or spread of a size class, and it is inversely proportional to the degree of sorting. The *Skewness* expresses the degree of symmetry in the distribution of the grains at the various dimensions. When the distribution is perfectly symmetric the *Skewness* is equal to 0, positive values are obtained when the slope of the cumulative curve towards the finer fractions is lower than the slope towards coarser grain size fractions, while it is negative in the opposite case. Finally, the *Kurtosis* is the ratio between the slope of the cumulative curve in its central part and the slope towards its ends. It therefore expresses the prevalence of the intermediate grain size fractions with respect to the extreme ones.

Based on the computed grain size parameters, high resolution images were also obtained with backscattered electrons at Electron Microscopy

and Microanalysis Laboratory of Earth Sciences Department of Sapienza University of Rome using a SEM FEI Quanta 400 with EDAX Genesis microanalysis system on selected samples to study grain morphology in relation to the transport process.

4.2. Oxygen and carbon stable isotopes

The oxygen and carbon stable isotope analysis of carbonate-bearing sediments were performed to provide information about the environmental conditions of the area surrounding the lake. As reported by Talbot (1990), in short-residence-time open lakes, carbonate and oxygen isotopic compositions are rather constant and strongly correlated to the bulk isotopic composition of inflow waters.

For this reason, changes in lake carbonate $\delta^{13}C$ values generally result from changes in biogenic productivity (e.g., Li and Ku, 1997). Because ^{12}C is preferentially partitioned into lake organic matter, an increase in biogenic productivity leads to a relative increase of ^{13}C in dissolved CO_2, which is taken up by carbonates that precipitate from lake water. Therefore, an increase of $\delta^{13}C$ values generally reflects an increase of lake biogenic productivity. Furthermore, higher $\delta^{18}O$ values are associated with increasing evaporation, because ^{16}O is preferentially removed from the water during evaporation (e.g., Meijers et al., 2020).

Carbonate samples were powdered and analyzed on a Kiel III Carbonate Device coupled to a Finnigan Delta Plus isotope ratio mass spectrometer at the IsoLab of the University of Washington. Measured values were corrected to the V-PDB scale using a suite of internal reference materials that have been calibrated to and span a similar range of NBS19, NBS18, L-SVEC, and IAEA-603; details of the data acquisition protocol are available in Tobin et al. (2011).

4.3. X-ray diffraction of clay minerals

X-ray diffraction (XRD) analysis of clay minerals was performed to evaluate changes in environmental conditions in Seymareh Lake. It is well known how the clay mineral assemblage in sedimentary basins depends on several factors: (i) composition of the source rock (Chamley, 1989), (ii) chemical and physical alteration depending on latitude and climate (Thiry, 2000), (iii) diagenetic overprint as result of sedimentary and tectonic burial (Aldega et al., 2018, 2021), and (iv) vertical movements of adjacent continental areas and water level changes (Adatte et al., 2002). In fact, they can be used as a proxy for determining climate and paleoweathering conditions of continental areas (Thiry, 2000; Aldega et al., 2020). Since the clay mineral assemblage in the Seymareh lacustrine basin has not been overprinted by post-depositional events and considering that the time scale of our observations does not allow for large vertical movements, the observed mineral assemblage provides insights into the composition of the sediment source area, as well as the climatic and environmental conditions.

The analysis was carried out at the Academic Laboratory of Basin Analysis (ALBA) of Roma Tre University with a Scintag X1 system (CuKα radiation). The tube current and the voltage were 30 mA and 40 kV, respectively. The <2 µm grain size fraction was separated from the bulk rock by centrifuging and sedimented on glass slides producing a thin aggregate of at least 3 mg of clay per cm^2. Such highly oriented samples were air-dried at room temperature overnight and then saturated in the ethylene-glycol atmosphere at 25 °C for 24 h. Air-dried and ethylene-glycol solvated specimens were scanned under the same conditions (step size of 0.05° 2θ counting time of 4 s per step) but with a different scanning range. The former was X-rayed from 1 to 48°2θ, the latter from 1 to 30°2θ. Quantitative estimation of clay minerals was performed by calculating peak diffraction areas and using mineral intensity factors as calibration constants (Moore and Reynolds, 1997). Non-clay minerals such as quartz, calcite, dolomite, albite, and hematite, observed in the X-ray patterns, were not converted into mineral concentrations, thus the semiquantitative analysis refers only to sheet silicate minerals.
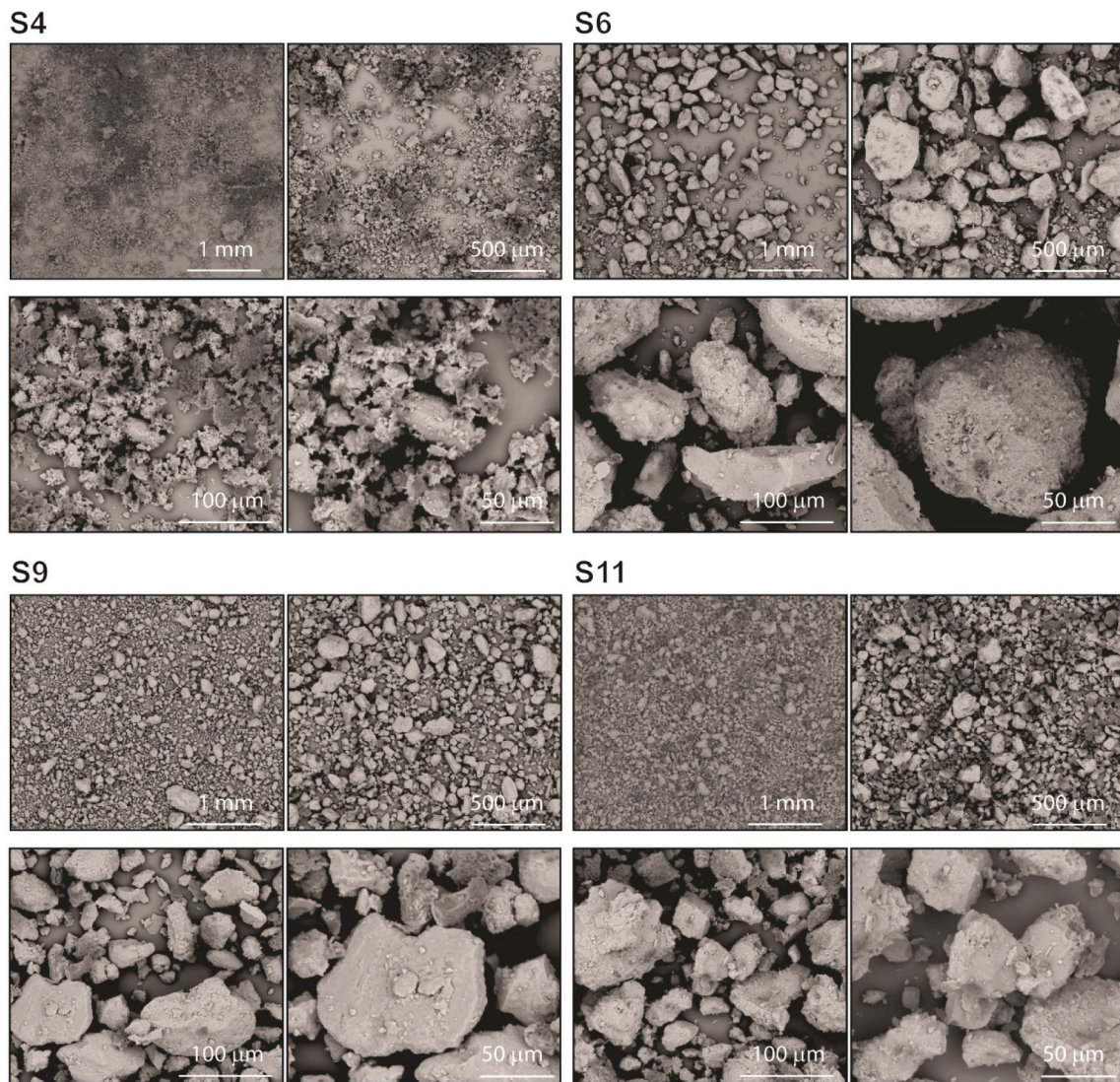
S4

S6

S9

S11

Fig. 5. High resolution backscattered electron images of S4, S6, S9 and S11 samples.

Table 3
Oxygen and carbon stable isotope results for the Seymareh lacustrine succession (see also Fig. 4).

Sample	$\delta^{18}O$		$\delta^{13}C$	
	Mean vs VPDB (permil)	StdDev vs VPDB (permil)	Mean vs VPDB (permil)	StdDev vs VPDB (permil)
S1	−5.21	0.03	−3.13	0.02
S2	−4.86	0.09	−3.69	0.04
S3	−6.05	0.02	−3.19	0.02
S4	−5.19	0.04	−3.21	0.02
S5	−5.08	0.02	−3.43	0.03
S6	−4.70	0.04	1.27	0.02
S7	−5.99	0.05	−3.83	0.02
S8	−5.74	0.03	−2.86	0.02
S9	−5.27	0.06	−3.45	0.02
S10	−4.97	0.02	−3.55	0.03
S11	−6.14	0.03	−3.08	0.02
S12	−4.83	0.03	−3.04	0.02
S13	−5.25	0.03	−3.67	0.02

Table 4
X-ray semiquantitative analysis of the Seymareh lacustrine succession. Acronyms: Plg = palygorskite; I = illite; C-S = mixed layers chlorite-smectite; Kln = kaolinite; Chl = chlorite.

Sample	Plg	<2 μm grain-size fraction (%wt.)			
		I	C-S	Kln	Chl
S1	18	30	22	14	15
S2	17	36	20	11	17
S3	25	40	13	9	13
S4	15	34	21	12	18
S5	22	38	11	14	15
S6	15	34	20	14	17
S7	20	34	22	11	13
S8	14	32	26	12	16
S9	17	36	18	13	16
S10	17	32	16	12	24
S11	18	33	21	13	16
S12	17	37	18	8	20
S13	18	29	15	18	21

4.4. Chronological model

A reconstruction of landscape evolution during the infilling and emptying of Seymareh Lake was carried out by using available published chronological data (Table 1). The age and the related elevation of lacustrine samples TO-13445 (9.73 ± 0.132 ka, Roberts and Evans,
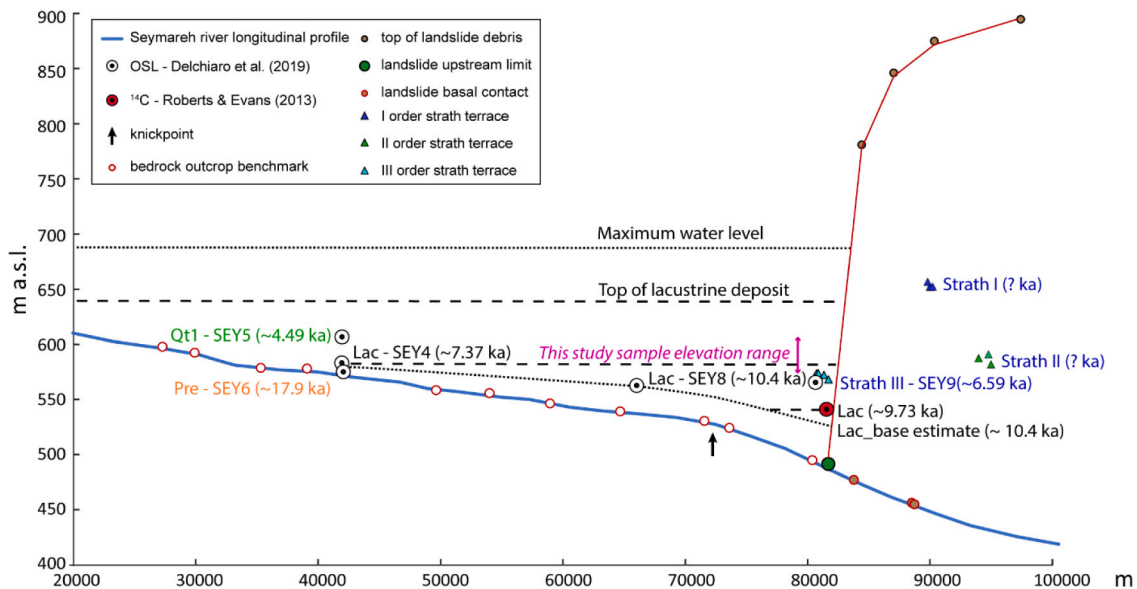
Fig. 6. Projection of chronological constraints from Table 1 along the longitudinal profile of the Seymareh River defining landforms and sedimentary deposits used as geomorphic markers (modified from after Delchiaro et al., 2019). The black dotted line refers to the reconstructed geometry of the basal contact of the lacustrine deposits, while the black dashed lines mark the intermediate and top lacustrine levels. The benchmarks of the basal contact of the Quaternary deposits on the bedrock, the projection of points joined by the red line corresponding to the top of the Seymareh landslide debris, and the upstream and downstream limits of the landslide are also reported.

2013), SEY8 (10.4 ± 0.90 ka, Delchiaro et al., 2019), SEY4 (7.37 ± 0.73 ka, Delchiaro et al., 2019) as well as the age of the III order strath terrace (SEY9: 6.59 ± 0.49 ka, Delchiaro et al., 2019) were used to build an Age-Elevation model.

The dated lacustrine levels are in the lower part of the lacustrine sequence between 540 and 590 m a.s.l. (TO-13445 and SEY4 respectively), while the top of the sequence at 630 m a.s.l. remains unconstrained. In this study we collected samples at elevations ranging from 580 to 610 m a.s.l. This stratigraphic interval overlaps with the dated sample at 590 m a.s.l. (7.37 ± 0.73 ka). Regarding the strath terrace sequence, the first and the second levels are not dated, while the third one at 570 m a.s.l. records the minimum age of the overflow event at 6.59 ± 0.49 ka. Then, the overflow age can be associated with the deposition of the top the lacustrine deposit at 630 m a.s.l., whose age is between 7.37 ± 0.73 and 6.59 ± 0.49 ka. For this reason, we can assume that the overflow age can be approximated to the average age of samples SEY4 and SEY9, which is equal to 6.98 ± 0.39 ka, where the error refers to the half of the temporal range between SEY4 and SEY9.

To build the chronological model, pre-lacustrine and lacustrine samples were projected along the longitudinal profile of the present trunk stream providing useful constraints to reconstruct the geometry of the basal surface of the lacustrine deposits, whose age is referred to SEY8 (10.4 ± 0.90 ka, Delchiaro et al., 2019). Then, median, maximum and minimum sedimentation and incision rates for the lake infilling and emptying phases respectively were obtained by computing four series of linear regressions of the elevation and the temporal ranges between two consecutive samples. From the Age-Elevation plot it was then possible to extrapolate the chronology of the lacustrine succession and the related errors based on the field of existence of the linear regressions. All the aforementioned assumptions are based on extensive field observations of the lacustrine sequence that allowed us to confirm the continuity and flatness of lacustrine layers in the study area (in the Supplementary material 1 photos of the lacustrine location in correspondence of the sampling point are reported).

## 5. Results

5.1. Grain size and SEM analyses

The stratigraphic column as well as grain size analysis results are shown in Table 2 and Fig. 4, while the grain size distribution curves are available in the Supplementary material 2.

The overall grain size distribution shows a total absence of gravel and a variable proportion of sand, silt, and clay throughout the section. The sand percentage is generally very low (1 % or <1 %) except for samples S3 (607 m a.s.l.), S6 (598 m a.s.l.), S7 (595 m a.s.l.), S8 (592 m a.s.l.), S9 (589 m a.s.l.) and S11 (583 m a.s.l.) where it is >18 %. The sand amount reaches its maximum value of 86 % in S6 (598 m a.s.l.). The average silt aliquot is about 39 %, with a minimum value of 7 % in S6 (598 m a.s.l.) and a maximum value of 56 % in S11 (583 m a.s.l.). The average clay content is about 41 %, with a minimum value of 6 % in S6 (598 m a.s.l.) and a maximum value of 64 % in S4 (605 m a.s.l.).

The maximum *Mean Size* is 0.15 mm (2.68 φ) in S6 while the lowest value of 0.0025 mm (8.62 φ) was found in S4 and S5. From S10 to S6 there is a progressive increase of mean size from 0.003 mm (8.36 φ) to 0.15 mm (2.68 φ). The *Standard Deviation* ranges from 1.50 φ to 2.97 φ. A progressive increase of standard deviation is recorded from S10 to S7 with values between 1.56 φ to 2.88 φ. The *Skewness* is positive in S11, S8, S7, S6 and S3 with a maximum value of 0.46. It is negative in the remaining samples with the lowest value of −0.52. A progressive increase of Skewness occurred from S10 to S6, with values increasing from −0.12 to 0.38. Finally, *Kurtosis* reaches its maximum value of 3.4 in S6 and its minimum value of 0.54 in S9. A progressive increase occurred from S9 to S6 from 0.54 to 3.4.

From the stratigraphy reported in Fig. 4 as well as from the parameter analysis reported in Table 2, it emerges that our dataset is characterized by extremely different depositional conditions. Hence, four samples (S4, S6, S9 and S11) were selected for SEM observations, as the most representative of such differences.

From the comparison of high-resolution SEM images in Fig. 5, the difference among grains between S6 and other samples is particularly evident. In fact, S6 is characterized by coarse and subangular grains with size >100 μm. S4 is characterized by the finest particle size with
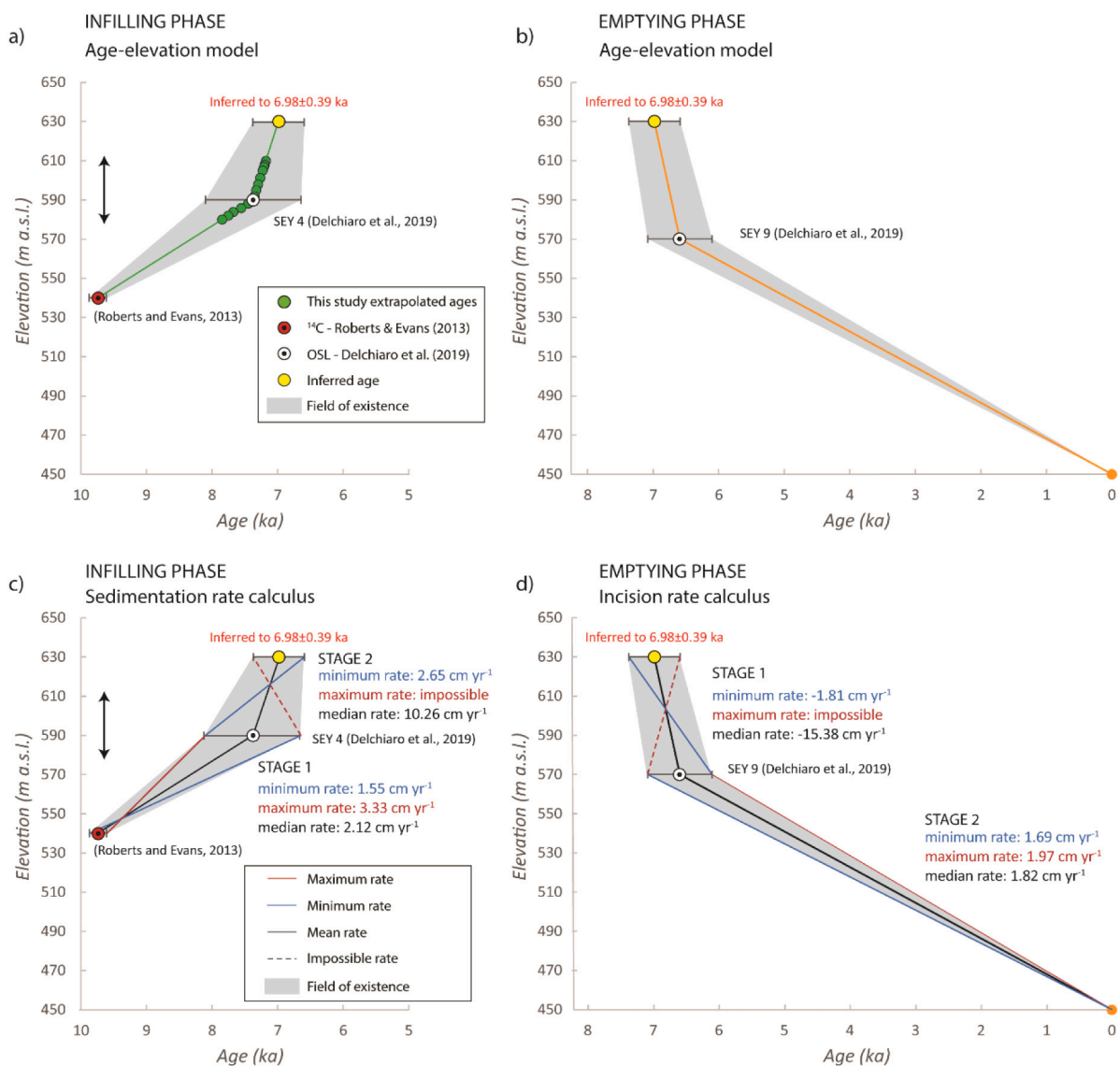
Fig. 7. Age-Elevation plots for the Seymareh Lake area related to the infilling (a) and the emptying (b) phases. Sedimentation rate (c) and incision rate (d) calculus models related respectively to the infilling and emptying phases. Chronological constraints are from OSL and ¹⁴C ages reported in Delchiaro et al. (2019) and Roberts and Evans (2013) in Table 1.
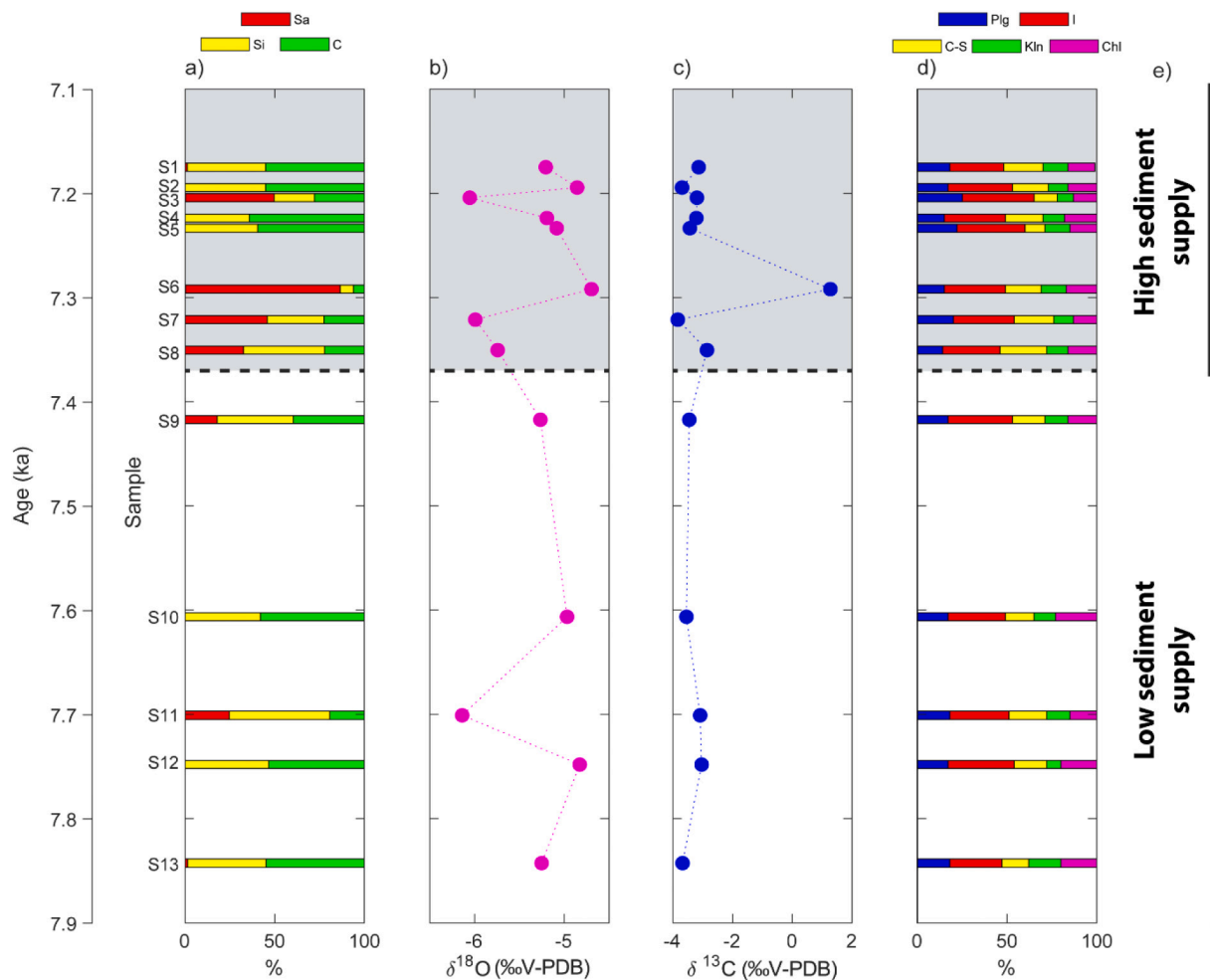
Table 5
Samples elevation and extrapolated ages with associated errors of the analyzed portion of the Seymareh lacustrine sequence. The linear extrapolation was performed considering the Age-Elevation model reported in Fig. 7.

Lake samples	Elevation (m a.s.l.)	Extrapolated age (ka)	Error (ka)
S1	610	7.18	0.56
S2	608	7.19	0.58
S3	607	7.20	0.59
S4	605	7.22	0.60
S5	604	7.23	0.61
S6	598	7.29	0.66
S7	595	7.32	0.69
S8	592	7.35	0.71
S9	589	7.42	0.72
S10	585	7.61	0.67
S11	583	7.70	0.65
S12	582	7.75	0.63
S13	580	7.84	0.61

numerous grains smaller than 50 μm to which clay minerals are adhered. Finally, S9 and S11 show quite similar characteristics, highlighting numerous grains with a size >50 μm to which clay minerals are adhered. Fossils and microfossils have been not observed in the samples.

5.2. Oxygen and carbon stable isotope

Oxygen and carbon stable isotope results are shown in Table 3 and in Fig. 9b and c, with further details available in the Supplementary material 3. The overall $\delta^{18}O$ values span from −6.14 ‰ to −4.70 ‰. The $\delta^{18}O$ distribution displays two consecutive negative trends from S10 (585 m a.s.l.) to S7 (595 m a.s.l.), where values decrease from −4.97 ‰ to −5.99 ‰, and from S5 (604 m a.s.l.) to S3 (607 m a.s.l.), where values decrease from −5.08 ‰ to −6.05 ‰. These trends are separated by the highest recorded $\delta^{18}O$ values in S6 (598 m a.s.l.) with −6.05 ‰. The overall $\delta^{13}C$ values of the Seymareh lacustrine succession span from −3.83 ‰ to +1.27 ‰. The $\delta^{13}C$ value distribution shows small scale variations ranging from −3.83 ‰ to −2.86 ‰, except for S6 (598 m a.s. l.) where the value is positive (+1.27 ‰).

Fig. 8. Multi-plot of the dataset obtained in this study and relative ages. From the left: a) grain size percentages, b) oxygen stable isotope data (maximum standard deviation is 0.09 permil), c) carbon stable isotope data (maximum standard deviation is 0.04 permil), d) clay mineral percentages and e) lake sedimentation rates. The dark dashed line at 7.37 ± 0.73 ka marks the increase in sedimentation rate. Sa = sand; Si = Silt; C=Clay; Plg = palygorskite; I = illite; C-S = mixed layers chlorite-smectite; Kln = kaolinite; Chl = chlorite.

5.3. X-ray diffraction of clay minerals

X-ray semiquantitative results of the investigated lacustrine succession are shown in Table 4 and in Fig. 9d. Illite is the most abundant clay mineral with amounts ranging from 29 % to 40 % (average value 34 %). Palygorskite content increases slightly from <20 % in samples S13–S6 (580–598 m a.s.l.) up to 25 % in samples S5–S1 (604–610 m a.s.l.). The percentage of mixed layers chlorite-smectite ranges from 11 % to 26 % whereas kaolinite varies from 8 % to 18 %. Finally, chlorite ranges from 13 % to 24 % with an average of 17 %.

5.4. Chronological model

As shown in Fig. 6 the dated geomorphic markers reported in Table 1, as well as the undated geomorphic features are projected along the longitudinal profile of the Seymareh River.

Fig. 6 also shows the maximum water level at about 690 m a.s.l. produced by the swath topographic profile of Fig. 3. Indeed, no shorelines or similar landforms are preserved in the Seymareh area making it impossible to reconstruct the evolution of the water level during the infilling phase in relation to the deposition of the lacustrine sediments. In addition, although the persistence of the lake system suggests it can be considered endorheic, it is difficult to estimate the amount of groundwater that infiltrated into the landslide debris before overflowing. For this reason, the maximum elevation likely reached by the water during

the overflow was extracted by considering the minimum elevation in the primary zone of the landslide debris where no fluvial erosion reshaped the landforms. Indeed, as can be seen in the swath profile of Fig. 3, at least four steps in the minimum elevation can be recognized. These correspond to the strath terrace sequence and the maximum water elevation reached during the overflow event.

Based on the chronological model of Fig. 7, it was possible to extrapolate the ages and associated errors of the lacustrine succession (Table 5). A linear extrapolation of the sample ages and associated errors was computed considering the elevation, the minimum, mean and maximum ages of TO-13445 and SEY4 samples and the inferred overflow age and elevation, as reconstructed from the Age-Elevation model of Fig. 7.

From the model, it is evident that the lake infilling phase was characterized by an increase in the median sedimentation rate from 2.12 cm yr^{-1}, between 9.73 ± 0.13 and 7.37 ± 0.73 ka, to 10.26 cm yr^{-1} between 7.37 ± 0.73 and 6.98 ± 0.39 ka. Similarly, the overflow event that triggered the emptying phase can be subdivided into two stages: from 6.98 ± 0.39 to 6.59 ± 0.49 ka where the median incision rate was 15.38 cm yr^{-1}, and from 6.59 ± 0.49 ka to the present where the median incision rate decreased to 1.82 cm yr^{-1}.

However, the uncertainty of the model shows a considerable variability in the different morpho-evolutionary stages. In fact, in the first infilling stage a minimum rate of 1.55 cm yr^{-1} and a maximum of 3.33 cm yr^{-1} was computed, while in the second infilling stage only the
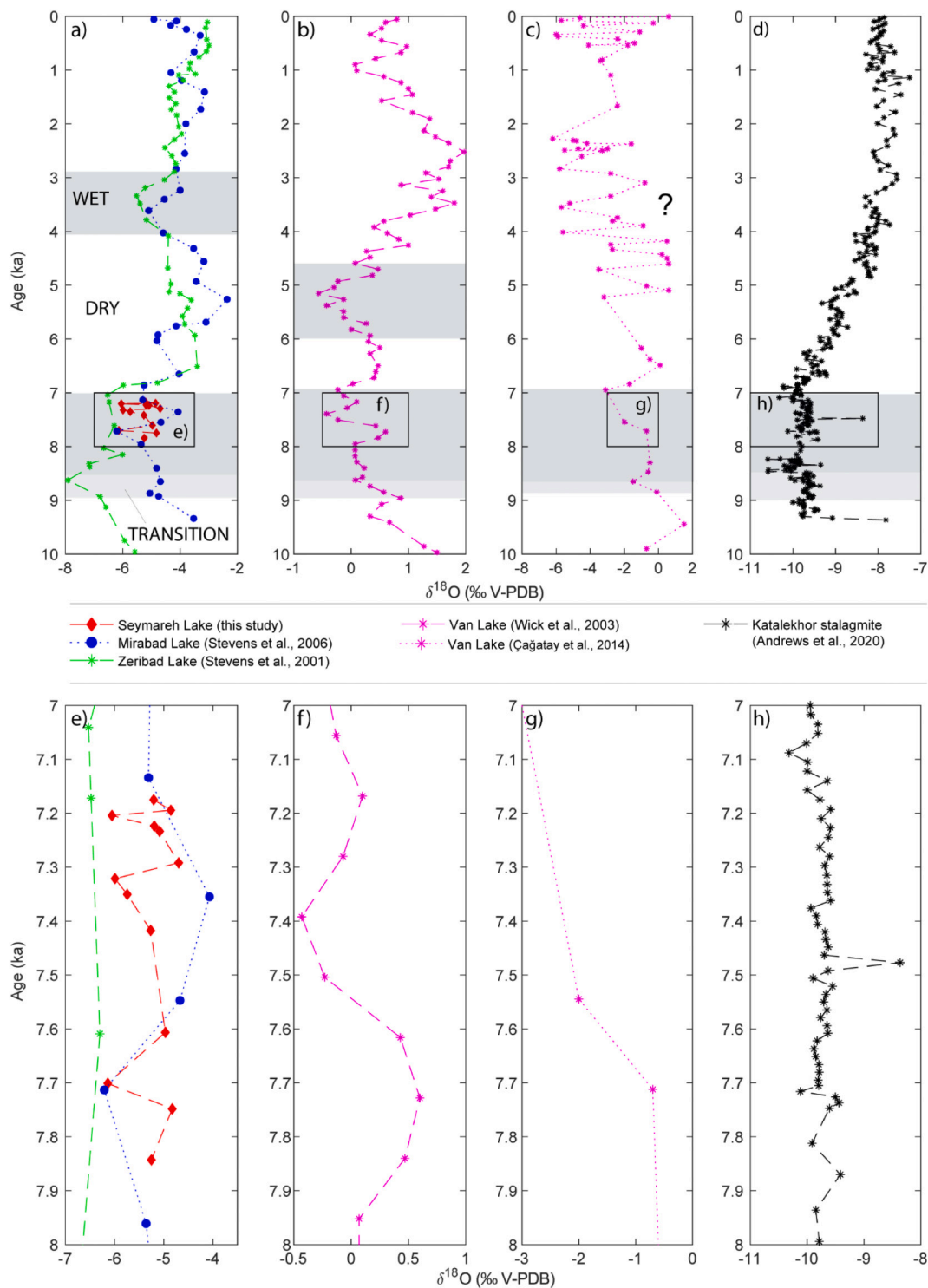
Fig. 9. A synoptic view of the main Holocene $\delta^{18}O$ based climatic reconstructions for the Zagros Mountains and neighboring areas: a) Mirabad Lake (Stevens et al., 2006), Zeribad Lake (Stevens et al., 2001), b, c) Van Lake (Wick et al., 2003; Çağatay et al., 2014), and d) Katalekhor stalagmite (Andrews et al., 2020). e, f, g, h) Focus of the $\delta^{18}O$ curves in the period from 8 to 7 ka.

minimum rate of 2.65 cm yr^{-1} can be extracted. The maximum rate, here, is impossible to define because the maximum age of the end of the infilling stage is older than that the minimum age of the start of the same stage (Fig. 7a and c). Regarding the emptying phase, the first stage has a minimum incision rate of 1.81 cm yr^{-1} and a maximum rate impossible to define because the minimum age of the beginning of the phase is younger than the maximum age of the end of the same phase (Fig. 7b and d). Finally, in the second stage of the emptying phase, a minimum

incision rate of 1.69 cm yr^{-1} and a maximum rate of 1.97 cm yr^{-1} were computed. The level of uncertainty is mainly because of the temporal overlap of the errors of the ages of the different samples and is strictly dependent on the dating method.
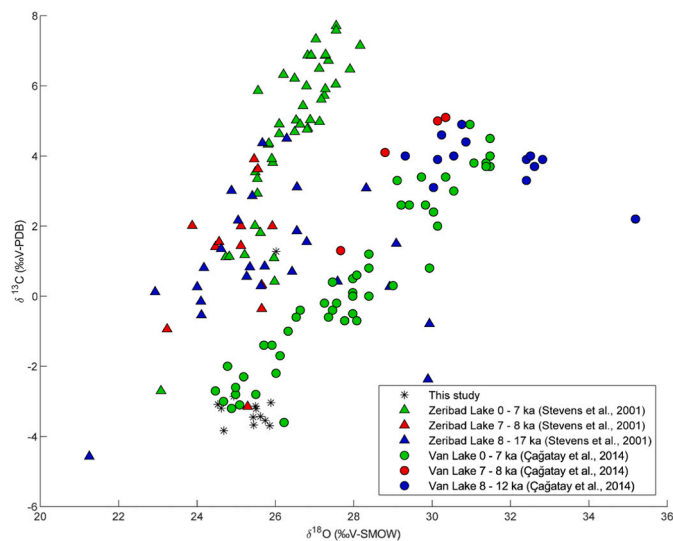
Fig. 10. $\delta^{18}O$ vs $\delta^{13}C$ data for Seymareh (this study), Zeribad (Stevens et al., 2001) and Van lakes (Çağatay et al., 2014).

5.5. Grain size, stable isotope and mineralogical trends during the lake infilling phase

The multi-plot of Fig. 8 shows that the analyzed portion of the lacustrine succession (S1–S13 samples) covers the period from 7.84 ± 0.61 to 7.18 ± 0.56 ka, likely recording the increase of the sedimentation rate starting at 7.37 ± 0.73 ka.

In the early-stage of the infilling phase, the sand content in the samples is low and only two samples (S11 – 7.70 ± 0.65 ka and S9 – 7.42 ± 0.72 ka) show higher sand amount (Fig. 8a). The $\delta^{18}O$ distribution displays that the negative trend from S10 (7.61 ± 0.67 ka) to S7 (7.32 ± 0.69 ka), where values decrease from −4.97 to −5.99 ‰, is between the two lake infilling periods (Fig. 8b). The distribution of $\delta^{13}C$ values illustrated in Fig. 8c is constant and the percentage of palygorskite in the early stage of the lake infilling phase oscillates around 18 % (Fig. 8d).

In the late stage of lake infilling, the increase of lacustrine sedimentation rate to a median value of 10.26 cm yr^{-1} is associated with

high input of sand. In detail, samples S9–S6 (7.42 ± 0.72 ka–7.29 ± 0.66 ka) show an exponential increase in sand contents with sample S6 having the highest percentage of the whole dataset (Fig. 8a). The $\delta^{18}O$ distribution displays part of the negative trend from S10 (7.61 ± 0.67 ka) to S7 (7.32 ± 0.69 ka), and another from S5 (7.23 ± 0.61 ka) to S3 (7.20 ± 0.59 ka), where values decrease from −5.08 to −6.05 ‰ (Fig. 8b). These trends are separated by the highest recorded $\delta^{18}O$ value in S6 (7.29 ± 0.66 ka) with −4.7 ‰. Considering the samples enriched in sand and the corresponding value of $\delta^{18}O$, we noticed that S11, S8, S7, and S3 have more negative values. The evolution of $\delta^{13}C$ illustrated in Fig. 8c is constant except for sample S6 (7.29 ± 0.66 ka) whose value is 1.27, much greater than the others. This spike correlates with the highest content of sand found in the lacustrine succession. Finally, the percentage of palygorskite amounts of in the late-stage phase increases to values up to 25 % (S3 - 7.20 ± 0.59 ka) (Fig. 8d).

6. Discussion

6.1. Regional paleoclimatic evolution (10–7 ka)

The dataset of the present study covers a short but crucial period (from 8 to 7 ka) and is here discussed in a broader temporal and geographical setting. Specifically, we compared our results with the main datasets available for the Zagros and the Anatolian-Iranian plateau to have a regional perspective for our interpretations on the past environmental conditions at Seymareh Lake. In Fig. 9 a synoptic view of the main Holocene $\delta^{18}O$ based climatic reconstructions is shown.

During the early Holocene (~10–9 ka), when the emplacement of the Seymareh landslide formed the dam lakes (Roberts and Evans, 2013; Shoaei, 2014; Delchiaro et al., 2019, 2020), dry climate conditions prevailed in the Middle East, as demonstrated by the $\delta^{18}O$ curves reported in Fig. 9 (Stevens et al., 2001; Wick et al., 2003; Stevens et al., 2006; Çağatay et al., 2014; Andrews et al., 2020). In addition, Griffiths et al. (2001) proposed that the early Holocene low-level phase in Mirabad Lake, located on the surface of Seymareh landslide debris, where shallow-water ostracods were detected, was related to the increase in water temperature and the abundance of winter precipitation. This is compatible with a continental regime characterized by one rainy season, as demonstrated also by pollen records for the Mirabad (Stevens et al., 2006), Zeribad (Stevens et al., 2001) and Van (Wasylikowa, 2005; Wasylikowa et al., 2006; Litt et al., 2014) lakes.
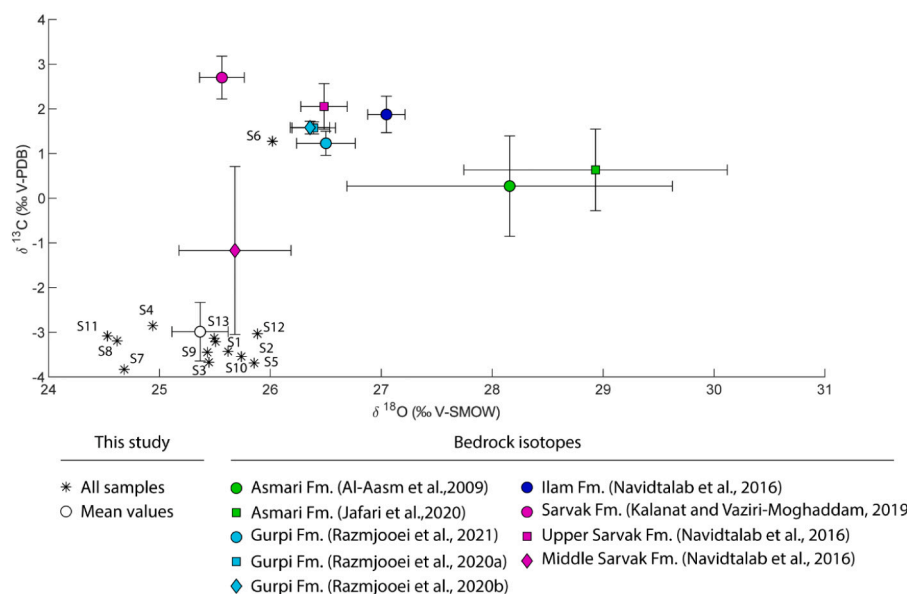

Fig. 11. $\delta^{18}O$ vs $\delta^{13}C$ plot in which Seymareh Lake (this study) result and those of the carbonate source formations in the Seymareh River basin (Al-Aasm et al., 2009; Navidtalab et al., 2016; Kalanat and Vaziri-Moghaddam, 2019; Jafari et al., 2020; Razmjooei et al., 2020a,b, 2021) are reported.
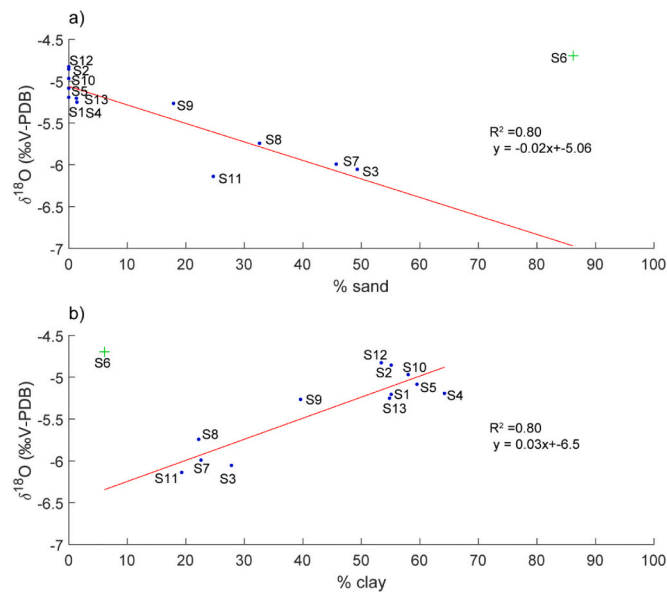
Fig. 12. Relationships between the grain classes (sand and clay) and the $\delta^{18}O$ concentrations.

At the end of the early Holocene (~9–8.5 ka), the continental dry conditions progressively shifted towards a wetter climate regime typical of the Mediterranean area, as recorded by more negative $\delta^{18}O$ values from Mirabad, Zeribad, Van and Katalekhor (Fig. 9; Stevens et al., 2001; Wick et al., 2003; Stevens et al., 2006; Çağatay et al., 2014; Andrews et al., 2020). However, during this period, pollen records (Stevens et al., 2001; Wasylikowa, 2005; Stevens et al., 2006; Wasylikowa et al., 2006; Litt et al., 2014) still highlight dry conditions, showing the delayed vegetation response to the climatic transition. Indeed, the highly drought tolerant *pistacia* prevailed over oak until 7 ka.

During the Mid Holocene (~8.5–7 ka), the Seymareh $\delta^{18}O$ values are similar to those observed in Zeribad (Stevens et al., 2001; Roberts et al., 2008), Mirabad (Griffiths et al., 2001; Stevens et al., 2006), Van (Wick et al., 2003; Çağatay et al., 2014) and Katalekhor (Andrews et al., 2020), indicating wetter climate conditions. Indeed, stable isotope values and clay mineral percentages from this study highlight a quite uniform and wet environmental context. Nevertheless, the abundance of benthic and shallow warm water assemblages of the ostracods from Mirabad Lake between 8 and 7 ka (Griffiths et al., 2001) suggests an unsteady climatic interval, consistent with the inference of the delayed vegetation response.

Afterwards, since 7 ka, the $\delta^{18}O$ curves of Zeribad (Stevens et al., 2001; Roberts et al., 2008), Mirabad (Griffiths et al., 2001; Stevens et al., 2006) and Van (Wick et al., 2003; Çağatay et al., 2014) lakes, and Katalekhor cave (Andrews et al., 2020), indicate a regional wet to dry climate transition. This is especially true for Mirabad and Zeribad lakes (Stevens et al., 2001, 2006), and Katalekhor stalagmite (Andrews et al., 2020), which recorded an increase of the heaviest isotope $\delta^{18}O$ in response to enhanced evaporation. Also, Van Lake (Wick et al., 2003; Litt et al., 2014) records an increase of $\delta^{18}O$, but just for the 7–6 ka period. Accordingly, Wick et al. (2003) pointed out that the transition towards drier climate conditions at Van Lake could be likely more influenced by the Siberian high-pressure prevalence.

6.2. Paleoclimatic and depositional energy conditions in the Seymareh Lake area (8–7 ka)

The $\delta^{18}O$ vs $\delta^{13}C$ plot of Fig. 10 shows a positive covariance between O and C isotopes that indicates a closed basin hydrology (Leng and Marshall, 2004; Meijers et al., 2020) for the Zeribad (Stevens et al., 2001) and Van (Çağatay et al., 2014) lakes.

According to the lake basin classification of Carroll and Bohacs (1999), a closed lake is characterized by limited surface or underground outflow, meaning that most water exits the lake through evaporation. Under such circumstances, lake levels respond to fluctuations in the amount of riverine input and evaporation.

Conversely, our dataset does not show any covariance likely because of its short time interval (i.e., 800 yr). However, our $\delta^{18}O$ values compared to $\delta^{18}O$ of the other datasets within the same period (8–7 ka) highlights a quite stable wet phase, characterized by low $\delta^{18}O$ values. In detail, our $\delta^{18}O$ values are consistent with $\delta^{18}O$ values of Zeribad Lake (Stevens et al., 2001), while $\delta^{18}O$ divergence of Van Lake can be likely caused by many factors, such as latitude, vapor source, elevation, carbonate mineralogy and in particular seasonality (Çağatay et al., 2014). Regarding carbon isotope, our dataset is characterized by low and homogenous values between −3.69 and −2.86, excepting for S6.

In this regard, we compare the $\delta^{18}O$ vs $\delta^{13}C$ results with oxygen and carbon isotope data of the lacustrine carbonates deposited in the Seymareh River basin (Al-Aasm et al., 2009; Navidtalab et al., 2016; Kalanat and Vaziri-Moghaddam, 2019; Jafari et al., 2020; Razmjooei et al., 2020a,b, 2021) (Fig. 11), and the $\delta^{18}O$ concentrations with the grain classes (sand, and clay) (Fig. 12). Importantly, our stable isotope data are different from available data of Meso-Cenozoic marine limestones exposed in the catchment of the Seymareh basin (Fig. 11). This indicates that the isotopic signature from the Holocene lacustrine deposits is most likely primary and not affected by detrital components of the source area. Therefore, stable isotope data could record the climatic and environmental conditions at the time of deposition. The only exception is represented by sample S6, whose $\delta^{18}O$ vs $\delta^{13}C$ values closer to the bedrock ones suggest a detrital origin likely caused by an increase in the sediment supply from sediment transport during surface runoff.

Although our dataset describes a stable wet phase between 8 and 7 ka, the lake infilling history indicates a gradual increase of the depositional system energy after 7.37 ± 0.73 ka.

In fact, as the sedimentation rate increases from a median value of 2.12 cm yr^{-1} to 10.26 cm yr^{-1} at 7.37 ± 0.73, sand content increases (S8, S7, S6, S3). Observing the relationships in Fig. 12, the sand class is inversely proportional to $\delta^{18}O$ content, while the clay class is directly proportional, suggesting that the high energy system prevails during the wetter phases (i.e., lower $\delta^{18}O$), where sand content is higher than the clay content (Ballato and Strecker, 2013). It means that after 7.37 ± 0.73 ka, local climate variations, characterized by a minor variability in the $\delta^{18}O$, enhanced sediment mobilization from the hillslopes to the lake system.

6.3. Effects on hillslope-lake system of local vs regional and short vs long term climate changes

Fig. 13 represents a schematic reconstruction of the hillslopes surrounding the Seymareh Lake system and their interactions with the lake water table until the overflow event. During the early Holocene (~10–9 ka), dry climate conditions favored regolith formation mainly by physical weathering, presumably because of the barren vegetation that partially covered the hillslopes (Fig. 13a) (Roberts, 2014). The low sediment input might be related to the occurrence of one-rainy season rainfall distribution that limited the sediment mobilization (Maltman and Bolton, 2003). The lake water level can be supposed to be low because of the dry climate conditions, as confirmed by the stable isotope composition of Mirabad Lake located close to the Seymareh Lake area (Stevens et al., 2006).

The transition to wetter climate conditions from ~9–7.4 ka led to an initial increase in the sediment supply from the hillslopes mobilized by the increase of precipitation amount and different distribution during the year (two rainy seasons) (Garcin et al., 2017; Tofelde et al., 2017). However, as the vegetation cover became denser over the hillslopes, the sediment supply is expected to be stabilized (Fig. 13b) (Gray, 1995; Garcin et al., 2017; Löbmann et al., 2020). During this period, the lake
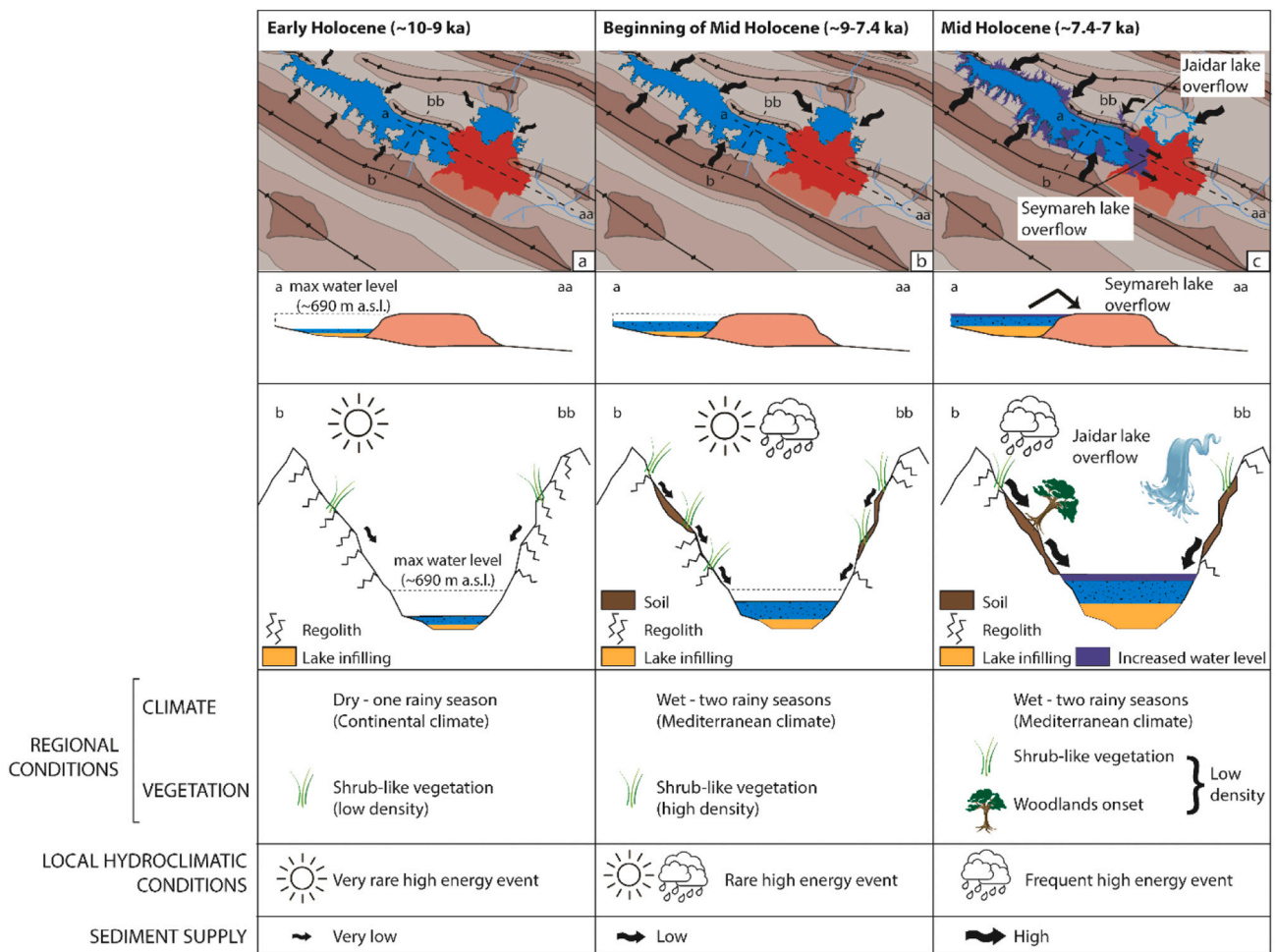
Fig. 13. Schematic reconstruction of hillslope-lake interaction. a) During the early Holocene the occurrence of a sparse shrub-like vegetation, and the continental climate characterized by one rainy season limited the sediment mobilization favoring the formation of regolith; b) At the end of the early Holocene the onset of wetter conditions and the different rainfall distribution (two rainy seasons) increase the sediment supply that stabilized as the vegetation became denser; c) At the beginning of the Middle Holocene, regional climatic conditions were the same of the previous phase, while vegetation became less dense, favoring hillslope erosion caused by local high hydroclimatic energy events that led to the overflow of Jaidar Lake into Seymareh Lake and to a further increase of the lake infilling that justifies the Seymareh overflow.

water level likely increased as the wetter conditions prevailed, as demonstrated also by the isotopic composition of the Mirabad Lake (Stevens et al., 2006) as well as the main datasets available for the Zagros and the Anatolian-Iranian plateau (Stevens et al., 2001; Wick et al., 2003; Çağatay et al., 2014; Andrews et al., 2020).

During the Mid Holocene (~7.4–7 ka), although the regional climatic conditions were explicitly wetter (two rainy seasons), pollen data from Zeribad Lake (Stevens et al., 2001; Wasylikowa, 2005) indicate a drastic reduction of shrubs (i.e., Pistacia) in conjunction with a slow appearance of woodlands (Quercus) resulting in the reduction of the vegetation cover percentage, with a sparse distribution over hillslopes. The decrease of the vegetation cover percentage allowed the previously formed soil to be easily mobilized through sheet and rill erosion (Gray, 1995; Löbmann et al., 2020), especially along the steep valley network. However, an unexpected increase of the median sedimentation rate from 2.12 cm yr^{-1} to 10.26 cm yr^{-1} occurred starting from ~7.4 ka. In this regard, local high energy events, characterized by high sand supply and low δ^{18}O concentration, were recorded more frequently (also observed in the grain size statistical analysis) where the increase of sand content between the S10 and S7 samples (~7.6–7.32 ka) is associated with poor sediment sorting, then becoming better sorted in S6 (~7.3 ka). In the same range, the asymmetry varies from a finer (S9) to a coarser distribution (S8–S6), while the *kurtosis* value indicates that the prevalence of

the intermediate classes increases greatly at sample S6, whose value is much higher than for the entire dataset. In this phase, the increase of lake water level remained the same as the previous phase but since the basin accommodation space decreased as the sediment supply increased, the maximum threshold elevation of 690 m a.s.l. was reached by the lake water level.

This is consistent with the hypothesis proposed by Shoaei (2014), that the Seymareh landslide dam overflow was caused by a domino effect: the overflow of Jaidar Lake into Seymareh Lake before the overflow of the latter. Because the Kashkan River flowed with high discharge into the smaller reservoir of Jaidar Lake, it led Jaidar Lake to overflow into Seymareh Lake.

Indeed, the high energy events from ~7.6–7.32 ka could justify a sudden increase of the tributaries' discharge that culminated at ~7.3 ka because of the complete overflow of Jaidar Lake into Seymareh Lake (Fig. 13c).

In this regard, we defined such high energy events as extreme hydrological events (sensu Gregory et al., 2006) of high magnitude related to the hydrological cycle (e.g., rainfall, runoff, snowmelt, flood, water recharge). Furthermore, the frequent occurrence of local high energy events from ~7.6–7.32 ka could be related to the progressive decrease of mid Holocene winter precipitation and a marked seasonal and interannual variability of rainfall (Andrews et al., 2020), that together with

the sparse vegetation on the hillslopes (Stevens et al., 2001; Wasyli-kowa, 2005), favored both Jaidar overflow and the lacustrine sedimentation of Seymareh Lake.

Finally, Benito et al. (2015) observed a significant spatial and temporal clustering of Holocene flooding episodes in the period 7.8–7.15 ka across the eastern Mediterranean region, reflecting different flood sensitivity to centennial-scale hydro-climatic changes. This bracket age is consistent with the Seymareh Lake overflow event highlighting it as a possible marker of the local effect of regional climate variations.

7. Conclusions

Overflowing of landslide-dam lakes is generally accepted as the main response of lake systems to variations in water discharge and sediment supply. In particular, the transition from dry to wet climate conditions enhances sediment mobilization along hillslopes and connected channel networks until the vegetation became denser, reducing the sediment supply. However, an unexpected increase of the median sedimentation rate from 2.12 cm yr^{-1} to 10.26 cm yr^{-1} occurred from ~7.4 ka in the Seymareh Lake area. In this regard, local high energy events related to the hydrological cycle were recorded more frequently. Progressively, the increased sedimentation rate produced a decrease in the accommodation space within the downstream lake basins that led to the overflow of Jaidar Lake into Seymareh Lake and to a further increase of the lake infilling that justifies the Seymareh overflow. Seymareh Lake provided new evidence of the combined influence of local vs. regional contributions, as well as short- vs long-term Holocene environmental changes on the timing of the evolution of landslide dammed lakes.

Overall, our multi-proxy analysis represents a suitable approach for identifying short- and long-term environmental changes occurred during the Holocene. Specifically, we showed how grain size distributions record the energy of the geomorphic system and hence represent a proxy for determining local and short-term environmental changes, while stable isotopes and X-ray diffraction analysis of clay minerals are useful tools for detecting regional and long-term climate changes. Finally, the 3000-yr-long sedimentary record of Seymareh Lake can be considered a geological archive documenting the Holocene environmental changes in the Middle East, and in turn, offering a suitable piece of information to untangle high-resolution environmental reconstructions.

Declaration of competing interest

The authors declare that they have no known competing financial interests or personal relationships that could have appeared to influence the work reported in this paper.

Appendix A. Supplementary data

Supplementary data to this article can be found online at https://doi.org/10.1016/j.geomorph.2022.108367.

References

Adatte, T., Kell, G., Stinnesbeck, W., 2002. Late cretaceous to early Paleocene climate and sea-level fluctuations: the Tunisian record. Palaeogeogr. Palaeoclimatol. Palaeoecol. 178 (3–4), 165–196. https://doi.org/10.1016/S0031-0182(01)00395-9.

Al-Aasm, I.S., Ghazban, F., Ranjbaran, M., 2009. Dolomitization and related fluid evolution in the Oligocene-Miocene Asmari Formation, Gachsaran area, SW Iran: petrographic and isotopic evidence. J. Pet. Geol. 32 (3), 287–304. https://doi.org/10.1111/j.1747-5457.2009.00449.x.

Agard, P., Omrani, J., Jolivet, L., Mouthereau, F., 2005. Convergence history across Zagros (Iran): constraints from collisional and earlier deformation. Int. J. Earth Sci. 94 (3), 401–419. https://doi.org/10.1007/s00531-005-0481-4.

Aldega, L., Bigi, S., Carminati, E., Trippetta, F., Corrado, S., Kavoosi, M.A., 2018. The Zagros fold-and-thrust belt in the Fars province (Iran): IIThermal evolution. Marine and Petroleum Geology 93, 376–390. https://doi.org/10.1016/j.marpetgeo.2018.03.022.

Aldega, L., Brandano, M., Cornacchia, I., 2020. Trophism, climate and paleoweathering conditions across the Eocene-Oligocene transition in the Massignano section (northern Apennines, Italy). Sediment. Geol. 405, 105701 https://doi.org/10.1016/j.sedgeo.2020.105701.

Aldega, L., Carminati, E., Scharf, A., Mattern, F., 2021. Thermal maturity of the Hawasina units and origin of the Batinah Mélange (Oman Mountains): Insights from clay minerals. Mar. Pet. Geol. 133, 105316 https://doi.org/10.1016/j.marpetgeo.2021.105316.

Alvioli, M., Melillo, M., Guzzetti, F., Rossi, M., Palazzi, E., von Hardenberg, J., Brunetti, M.T., Peruccacci, S., 2018. Implications of climate change on landslide hazard in Central Italy. Sci. Total Environ. 630, 1528–1543. https://doi.org/10.1016/j.scitotenv.2018.02.315.

Andrews, J.E., Carolin, S.A., Peckover, E.N., Marca, A., Al-Omari, S., Rowe, P.J., 2020. Holocene stable isotope record of insolation and rapid climate change in a stalagmite from the Zagros of Iran. Quaternary Sci. Rev. 241, 106433 https://doi.org/10.1016/j.quascirev.2020.106433.

ASTM, 2007. 422-63. Standard test method for particle-size analysis of soils. In: Annual Book of ASTM Standards, 4, pp. 10–16.

Ballato, P., Strecker, M.R., 2013. Assessing tectonic and climatic causal mechanisms in foreland-basin stratal architecture: insights from the Alborz Mountains, northern Iran. Earth Surf. Process. Landf. 39 (1), 110–125. https://doi.org/10.1002/esp.3480.

Benito, G., Macklin, M.G., Zielhofer, C., Jones, A.F., Machado, M.J., 2015. Holocene flooding and climate change in the Mediterranean. Catena 130, 13–33. https://doi.org/10.1016/j.catena.2014.11.014.

Bigi, S., Carminati, E., Aldega, L., Trippetta, F., Kavoosi, M.A., 2018. Zagros fold and thrust belt in the Fars province (Iran) I: Control of thickness/rheology of sediments and pre-thrusting tectonics on structural style and shortening. Mar. Pet. Geol. 91, 211–224. https://doi.org/10.1016/j.marpetgeo.2018.01.005.

Boutoux, A., Briaud, A., Faccenna, C., Ballato, P., Rossetti, F., Blanc, E., 2021. Slab folding and surface deformation of the Iran mobile belt. Tectonics 40 (6), e2020TC006300. https://doi.org/10.1029/2020TC006300.

Burbank, D.W., Anderson, R.S., 2011. Tectonic geomorphology. John Wiley & Sons.

Çağatay, M.N., Öğretmen, N., Damcı, E., Stockhecke, M., Sancar, Ü., Eriş, K.K., Özeren, S., 2014. Lake level and climate records of the last 90 ka from the Northern Basin of Lake Van, eastern Turkey. Quat. Sci. Rev. 104, 97–116. https://doi.org/10.1016/j.quascirev.2014.09.027.

Carroll, A.R., Bohacs, K.M., 1999. Stratigraphic classification of ancient lakes: Balancing tectonic and climatic controls. Geology 27 (2), 99–102. https://doi.org/10.1130/0091-7613(1999)027<0099:SCOALB>2.3.CO;2.

Casciello, E., Vergés, J., Saura, E., Casini, G., Fernández, N., Blanc, E., Homke, S., Hunt, D.W., 2009. Fold patterns and multilayer rheology of the Lurestan Province, Zagros simply folded belt (Iran). J. Geol. Soc. 166 (5), 947–959. https://doi.org/10.1144/0016-76492008-138.

Chamley, H., 1989. Clay formation through weathering. In: Clay Sedimentology. Springer, Berlin, Heidelberg, pp. 21–50. https://doi.org/10.1007/978-3-642-85916-8_2.

Clague, J.J., Evans, S.G., 2000. A review of catastrophic drainage of moraine-dammed lakes in British Columbia. Quaternary Sci. Rev. 19, 1763–1783. https://doi.org/10.1016/S0277-3791(00)00090-1.

Collison, A., Wade, S., Griffiths, J., Dehn, M., 2000. Modelling the impact of predicted climate change on landslide frequency and magnitude in SE England. Eng. Geol. 55 (3), 205–218. https://doi.org/10.1016/S0013-7952(99)00121-0.

Costa, J.E., Schuster, R.L., 1988. The formation and failure of landslide dams. Bull. Geol. Soc. Am. 100, 1054–1068. https://doi.org/10.3133/ofr87392.

Costa, C.H., Díaz, E.G., 2007. Age constraints and paleoseismic implication of rock avalanches in the northern Patagonian AndesArgentina. J. S. Am. Earth Sci. 24, 48–57. https://doi.org/10.1016/j.jsames.2007.03.001.

Crozier, M.J., 2010. Deciphering the effect of climate change on landslide activity: a review. Geomorphology 124, 260–267. https://doi.org/10.1016/j.geomorph.2010.04.009.

Delchiaro, M., Della Seta, M., Martino, S., Dehbozorgi, M., Nozaem, R., 2019. Reconstruction of river valley evolution before and after the emplacement of the giant Seymareh rock avalanche (Zagros Mts., Iran). Earth Surf. Dyn. 7, 929–947. https://doi.org/10.5194/esurf-7-929-2019.

Delchiaro, M., Rouhi, J., Della Seta, M., Martino, S., Nozaem, R., Dehbozorgi, M., 2020. The Giant Seymareh Landslide (Zagros Mts., Iran): A Lesson for Evaluating Multi-temporal Hazard Scenarios. In: De Maio, M., Tiwari, A. (Eds.), Applied Geology. Springer, Cham, pp. 209–225. https://doi.org/10.1007/978-3-030-43953-8_13.

Ermini, L., Casagli, N., 2003. Prediction of the behaviour of landslide dams using a geomorphological dimensionless index. Earth Surf. Process. Landf. 28 (1), 31–47. https://doi.org/10.1002/esp.424.

Evans, J.P., Smith, R.B., 2006. Water vapor transport and the production of precipitation in the eastern Fertile Crescent. J. Hydrometeorol. 7 (6), 1295–1307. https://doi.org/10.1175/JHM550.1.

Fan, X., Dufresne, A., Subramanian, S.S., Strom, A., Hermanns, R., Stefanelli, C.T., Hewitt, K., Yunus, A.P., Dunning, S., Capra, L., Geertsema, M., Miller, B., Casagli, N., Jansen, J.D., Xu, Q., 2020. The formation and impact of landslide dams–state of the art. Earth-Sci. Rev. 203, 103116 https://doi.org/10.1016/j.earscirev.2020.103116.

Farr, T.G., Rosen, P.A., Caro, E., Crippen, R., Duren, R., Hensley, S., Kobrick, M., Paller, M., Rodriguez, E., Roth, L., Seal, D., Shaffer, S., Shimada, J., Umland, J., Werner, M., Oskin, M., Burbank, D., Alsdorf, D., 2007. The shuttle radar topography mission. Rev. Geophys. 45 https://doi.org/10.1029/2005RG000183.

Folk, R.L., Ward, W.C., 1957. Brazos River bar [Texas]; a study in the significance of grain size parameters. J. Sediment. Res. 27 (1), 3–26. https://doi.org/10.1306/74D70646-2B21-11D7-8648000102C1865D.

Garcin, Y., Schildgen, T.F., Acosta, V.T., Melnick, D., Guillemoteau, J., Willenbring, J., Strecker, M.R., 2017. Short-lived increase in erosion during the African Humid Period: evidence from the northern Kenya Rift. Earth Planet. Sci. Lett. 459, 58–69. https://doi.org/10.1016/j.epsl.2016.11.017.

Gray, D.H., 1995. Influence of vegetation on the stability of slopes. In: Barker, D.H. (Ed.), Vegetation and Slopes: Stabilization, Protection and Ecology, Proceedings of the International Conference Held at the University Museum, pp. 2–25. Oxford (1995).

Gregory, K.J., Benito, G., Dikau, R., Golosov, V., Johnstone, E., Jones, A.J.J., Macklin, M. G., Parsons, A.J., Passmore, D.G., Poesen, J., Soja, R., Starkel, L., Thorndycraft, V.R., Walling, D.E., 2006. Past hydrological events and global change. Hydrol. Process. 20, 199–204. https://doi.org/10.1002/hyp.6105.

Griffiths, H.I., Schwalb, A., Stevens, L.R., 2001. Environmental change in southwestern Iran: the Holocene ostracod fauna of Lake Mirabad. The Holocene 11, 757–764. https://doi.org/10.1191/09596830195771.

Harris, I., Osborn, T.J., Jones, P., Lister, D., 2020. Version 4 of the CRU TS monthly high-resolution gridded multivariate climate dataset. Sci. Data 7 (1), 1–18. https://doi.org/10.1038/s41597-020-0453-3.

Harrison, S., Kargel, J.S., Huggel, C., Reynolds, J., Shugar, D.H., Betts, R.A., Emmer, A., Glasser, N., Haritashya, U.K., Klimeš, J., Reinhardt, L., Schaub, Y., Wiltshire, A., Regmi, D., Vilímek, V., 2018. Climate change and the global pattern of moraine-dammed glacial lake outburst floods. Cryosphere 12 (4), 1195–1209. https://doi.org/10.5194/tc-12-1195-2018.

Heidarzadeh, G., Ballato, P., Hassanzadeh, J., Ghassemi, M.R., Strecker, M.R., 2017. Lake overspill and onset of fluvial incision in the Iranian Plateau: insights from the Mianeh Basin. Earth Planet. Sci. Lett. 469, 135–147. https://doi.org/10.1016/j.epsl.2017.04.019.

Hermanns, R.L., Niedermann, S., Ivy-Ochs, S., Kubik, P.W., 2004. Rock avalanching into a landslide-dammed lake causing multiple dam failure in Las Conchas valley (NW Argentina)-evidence from surface exposure dating and stratigraphic analyses. Landslides 1, 113–122. https://doi.org/10.1007/s10346-004-0013-5.

Huggel, C., Clague, J.J., Korup, O., 2012. Is climate change responsible for changing landslide activity in high mountains? Earth Surf. Proc. Land. 37, 77–91. https://doi.org/10.1002/esp.2223.

Kalanat, B., Vaziri-Moghaddam, H., 2019. The Cenomanian/Turonian boundary interval deep-sea deposits in the Zagros Basin (SW Iran): bioevents, carbon isotope record and palaeoceanographic model. Palaeogeogr. Palaeoclimatol. Palaeoecol. 533, 109238 https://doi.org/10.1016/j.palaeo.2019.109238.

Kehl, M., 2009. Quaternary climate change in Iran - the state of knowledge. Erdkunde 63, 1–17. https://doi.org/10.3112/erdkunde.2009.01.01.

Köppen, W., 1900. Versuch einer Klassifikation der Klimate, vorzugsweise nach ihren Beziehungen zur Pflanzenwelt. Geographische Zeitschrift 6 (11. H), 593–611.

Korup, O., 2002. Recent research on landslide dams-a literature review with special attention to New Zealand. Prog. Phys. Geogr. 26 (2), 206–235. https://doi.org/10.1191/0309133302 pp333ra.

Jafari, J.A.L.I.L., Mahboubi, A., Moussavi-Harami, R., Al-Aasm, I.S., 2020. The effects of diagenesis on the petrophysical and geochemical attributes of the Asmari Formation, Marun oil field, Southwest Iran. Pet. Sci. 17 (2), 292–316. https://doi.org/10.1007/s12182-019-00421-0.

James, G.A., Wynd, J.G., 1965. Stratigraphic nomenclature of Iranian oil consortium agreement area. AAPG Bull. 49 (12), 2182–2245. https://doi.org/10.1306/A663388A-16C0-11D7-8645000102C1865D.

Leng, M.J., Marshall, J.D., 2004. Palaeoclimate interpretation of stable isotope data from lake sediment archives. Quat. Sci. Rev. 23 (7–8), 811–831. https://doi.org/10.1016/j.quascirev.2003.06.012.

Li, H.C., Ku, T.L., 1997. δ13C–δ18C covariance as a paleohydrological indicator for closed-basin lakes. Palaeogeogr. Palaeoclimatol. Palaeoecol. 133 (1–2), 69–80. https://doi.org/10.1016/S0031-0182(96)00153-8.

Litt, T., Pickarski, N., Heumann, G., Stockhecke, M., Tzedakis, P.C., 2014. A 600,000 year long continental pollen record from Lake Van, eastern Anatolia (Turkey). Quat. Sci. Rev. 104, 30–41. https://doi.org/10.1016/j.quascirev.2014.03.017.

Llewellyn, P.G., 1974. Palganeh. 1:100 000 Geological Map. Iran Oil Operating Companies, Geological Exploration Division, Tehran, Iran.

Löbmann, M.T., Geitner, C., Wellstein, C., Zerbe, S., 2020. The influence of herbaceous vegetation on slope stability - a review. Earth-Sci. Rev. 209, 103328 https://doi.org/10.1016/j.earscirev.2020.103328.

Macleod, J.H., 1970. Kabir kuh. 1:100 000 Geological Map. Iran Oil Operating Companies, Geological Exploration Division, Tehran, Iran.

Macleod, J.H., Fozoonmayh, M., 1970. Naft. 1:100 000 Geological Map. Iran Oil Operating Companies, Geological Exploration Division, Tehran, Iran.

Macleod, J.H., Roohi, M., 1970. Kuh-e Varzarin. 1:100 000 Geological Map. Iran Oil Operating Companies, Geological Exploration Division, Tehran, Iran.

Maltman, A.J., Bolton, A., 2003. How sediments become mobilized. Geol. Soc. Lond., Spec. Publ. 216 (1), 9–20. https://doi.org/10.1144/GSL.SP.2003.216.01.02.

McQuarrie, N., 2004. Crustal scale geometry of the Zagros fold–thrust belt Iran. Journal of Structural Geology 26 (3), 519–535. https://doi.org/10.1016/j.jsg.2003.08.009.

Meijers, M.J., Brocard, G.Y., Whitney, D.L., Mulch, A., 2020. Paleoenvironmental conditions and drainage evolution of the central Anatolian lake system (Turkey) during late Miocene to Pliocene surface uplift. Geosphere 16 (2), 490–509. https://doi.org/10.1130/GES02135.1.

Moore, D.M., Reynolds Jr., R.C., 1997. X-Ray Diffraction and the Identification and Analysis of Clay Minerals, second ed. Oxford University Press (OUP), USA.

Mouthereau, F., Lacombe, O., Vergés, J., 2012. Building the Zagros collisional orogen: timing, strain distribution and the dynamics of Arabia/Eurasia plate convergence. Tectonophysics 532, 27–60. https://doi.org/10.1016/j.tecto.2012.01.022.

Navidtalab, A., Rahimpour-Bonab, H., Huck, S., Heimhofer, U., 2016. Elemental geochemistry and strontium-isotope stratigraphy of Cenomanian to Santonian neritic carbonates in the Zagros Basin, Iran. Sedimentary Geology 346, 35–48. https://doi.org/10.1016/j.sedgeo.2016.10.003.

O'Connor, J.E., Costa, J.E., 2004. Spatial distribution of the largest rainfall-runoff floods from basins between 2.6 and 26,000 km2 in the United States and Puerto Rico. Water Resour. Res. 40 (1) https://doi.org/10.1029/2003WR002247.

Ouimet, W.B., Whipple, K.X., Royden, L.H., Sun, Z., Chen, Z., 2007. The influence of large landslides on river incision in a transient landscape: Eastern margin of the Tibetan Plateau (Sichuan, China). Geol. Soc. Am. Bull. 119, 1462–1476. https://doi.org/10.1130/B26136.1.

Pánek, T., 2019. Landslides and Quaternary climate changes—the state of the art. Earth Sci. Rev. 196, 102871 https://doi.org/10.1016/j.earscirev.2019.05.015.

Razmjooei, M.J., Thibault, N., Kani, A., Ullmann, C.V., Jamali, A.M., 2020a. Santonian-Maastrichtian carbon-isotope stratigraphy and calcareous nannofossil biostratigraphy of the Zagros Basin: long-range correlation, similarities and differences of carbon-isotope trends at global scale. Glob. Planet. Chang. 184, 103075 https://doi.org/10.1016/j.gloplacha.2019.103075.

Razmjooei, M.J., Thibault, N., Kani, A., Dinarès-Turell, J., Pucéat, E., Chin, S., 2020b. Calcareous nannofossil response to late cretaceous climate change in the eastern Tethys (Zagros Basin, Iran). Palaeogeogr. Palaeoclimatol. Palaeoecol. 538, 109418 https://doi.org/10.1016/j.palaeo.2019.109418.

Razmjooei, M.J., Shahryari, S., Kani, A., Ullmann, C.V., Jamali, A.M., Rahimi, S., Vergés, J., Thibault, N., 2021. Integrated bio-and carbon isotope stratigraphy of the Campanian–Danian sedimentary succession in Lurestan (Zagros Basin, Iran): Implications for syntectonic facies distribution and basin evolution. Journal of Asian Earth Sciences 214, 104779. https://doi.org/10.1016/j.jseaes.2021.104779 lanetary Change, 184, 103075.

Roberts, N., 2014. The Holocene: An Environmental History, third ed. Wiley-Blackweel, UK.

Roberts, N., Jones, M.D., Benkaddour, A., Eastwood, W.J., Filippi, M.L., Frogley, M.R., Lamb, H.F., Leng, M.J., Reed, J.M., Stein, M., Stevens, L., Valero, Garcès B., Zanchetta, G., 2008. Stable isotope records of late Quaternary climate and hydrology from Mediterranean lakes: the ISOMED synthesis. Quaternary Sci. Rev. 27 (25–26), 2426–2441. https://doi.org/10.1016/j.quascirev.2008.09.005.

Roberts, N.J., Evans, S.G., 2013. The gigantic Seymareh (Saidmarreh) rock avalanche, Zagros Fold-Thrust BeltIran. J. Geol. Soc. 170, 685–700. https://doi.org/10.1144/jgs2012-090.

Rouhi, J., Delchiaro, M., Della Seta, M., Martino, S., 2019. Emplacement kinematics of the Seymareh Rock-Avalanche Debris (Iran) inferred by field and remote surveying. Ital. J. Eng. Environ. 99–104 https://doi.org/10.4408/IJEGE.2019-01.S-16.

Rouhi, J., Delchiaro, M., Della, Seta M., Martino, S., 2022. New insights on the emplacement kinematics of the Seymareh landslide (Zagros Mts., Iran) through a novel spatial statistical approach. In: Front. Earth Sci.. https://doi.org/10.3389/feart.2022.869391.

Savelli, D., Troiani, F., Brugiapaglia, E., Calderoni, G., Cavitolo, P., Dignani, A., Ortu, E., Teodori, S., Veneri, F., Nesci, O., 2013. The landslide-dammed paleolake of Montelago (North Marche Apennines, Italy): Geomorphological evolution and paleoenvironmental outlines. Geogr. Fis. Dinam. Quat. 36, 267–287. https://doi.org/10.4461/GFDQ.2013.36.22.

Sherkati, S., Letouzey, J., Frizon de Lamotte, D., 2006. Central Zagros fold-thrust belt (Iran): New insights from seismic data, field observation, and sandbox modeling. Tectonics 25 (4). https://doi.org/10.1029/2004TC001766.

Shoaei, Z., 2014. Mechanism of the giant Seimareh Landslide, Iran, and the longevity of its landslide dams. Environ. Earth Sci. 72, 2411–2422. https://doi.org/10.1007/s12665-014-3150-8.

Stampfli, G.M., Borel, G.D., 2002. A plate tectonic model for the Paleozoic and Mesozoic constrained by dynamic plate boundaries and restored synthetic oceanic isochrons. Earth Planet. Sci. Lett. 196 (1–2), 17–33. https://doi.org/10.1016/S0012-821X(01)00588-X.

Stefanelli, C.T., Segoni, S., Casagli, N., Catani, F., 2016. Geomorphic indexing of landslide dams evolution. Eng. Geol. 208, 1–10. https://doi.org/10.1016/j.enggeo.2016.04.024.

Stevens, L.R., Wright Jr., H.E., Ito, E., 2001. Proposed changes in seasonality of climate during the Lateglacial and Holocene at Lake ZeribarIran. Holocene 11, 747–755. https://doi.org/10.1191/09596830195762.

Stevens, L.R., Ito, E., Schwalb, A., Wright Jr., H.E., 2006. Timing of atmospheric precipitation in the Zagros Mountains inferred from a multi-proxy record from Lake MirabadIran. Quaternary Res. 66, 494–500. https://doi.org/10.1016/j.yqres.2006.06.008.

Stuiver, M., Reimer, P.J., Bard, E., Beck, J.W., Burr, G.S., Hughen, K.A., Kromer, B., McCormac, F.G., Plicht, J.V.D., Spurk, M., 1998. INTCAL98 radiocarbon age calibration, 24,000-0 cal BP. Radiocarbon 40, 1041–1083. https://doi.org/10.1017/S0033822200019123.

Talbot, M.R., 1990. A review of the palaeohydrological interpretation of carbon and oxygen isotopic ratios in primary lacustrine carbonates. Chem. Geol. 80, 261–279. https://doi.org/10.1016/0168-9622(90)90009-2.

Talbot, C.J., Alavi, M., 1996. The past of a future syntaxis across the Zagros. Geol. Soc. Lond., Spec. Publ. 100 (1), 89–109. https://doi.org/10.1144/GSL.SP.1996.100.01.08.

Thiry, M., 2000. Palaeoclimatic interpretation of clay minerals in marine deposits: an outlook from the continental origin. Earth Sci. Rev. 49 (1–4), 201–221. https://doi.org/10.1016/S0012-8252(99)00054-9.

Tobin, T.S., Schauer, A.J., Lewarch, E., 2011. Alteration of micromilled carbonate $\delta 18O$ during Kiel device analysis. Rapid Commun. Mass Spectrom. 25 (15), 2149–2152. https://doi.org/10.1002/rcm.5093.

Tofelde, S., Schildgen, T.F., Savi, S., Pingel, H., Wickert, A.D., Bookhagen, B., Wittmann, H., Alonso, R.N., Cottle, J., Strecker, M.R., 2017. 100 kyr fluvial cut-and-fill terrace cycles since the Middle Pleistocene in the southern Central Andes, NW Argentina. Earth Planet. Sci. Lett. 473, 141–153. https://doi.org/10.1016/j.epsl.2017.06.001.

Vergés, J., Goodarzi, M.G.H., Emami, H., Karpuz, R., Efstathiou, J., Gillespie, P., 2011. Multiple Detachment Folding in Pusht-e Kuh Arc, Zagros: Role of Mechanical Stratigraphy. https://doi.org/10.1306/13251333M942899.

Watson, R.A., Wright, H.E., 1969. The Saidmarreh landslide, Iran, United States contributions to quaternary research, Geological Society of America, Special Papers. In: Schumm, S.A., Bradley, W.C. (Eds.), Papers Prepared on the Occasion of the VIII Congress of the International Association for Quaternary Research, Paris, France, 123, pp. 115–139.

Wasylikowa, K., 2005. Palaeoecology of Lake Zeribar, Iran, in the Pleniglacial, Lateglacial and Holocene, reconstructed from plant macrofossils. The Holocene 15, 720–735. https://doi.org/10.1191/0959683605hl846rp.

Wasylikowa, K., Witkowski, A., Walanus, A., Hutorowicz, A., Alexandrowicz, S.W., Langer, J.J., 2006. Palaeolimnology of Lake Zeribar, Iran, and its climatic implications. Quat. Res. 66, 477–493. https://doi.org/10.1016/j.yqres.2006.06.006.

Wick, L., Lemcke, G., Sturm, M., 2003. Evidence of late glacial and Holocene climatic change and human impact in eastern Anatolia: high-resolution pollen, charcoal, isotopic and geochemical records from the laminated sediments of Lake Van, Turkey. The Holocene 13, 665–675. https://doi.org/10.1191/0959683603hl653rp.

Wu, L.Z., Zhao, D.J., Zhu, J.D., Peng, J.B., Zhou, Y., 2020. A late Pleistocene river-damming landslide, Minjiang River, China. Landslides 17, 433–444. https://doi.org/10.1007/s10346-019-01305-5.

Zhong, Q., Wang, L., Chen, S., Chen, Z., Shan, Y., Zhang, Q., Ren, Q., Mei, S., Jiang, J., Hu, L., Liu, J., 2021. Breaches of embankment and landslide dams-State of the art review. Earth Sci. Rev. 103597 https://doi.org/10.1016/j.earscirev.2021.103597.